PHYSICAL REVIEW A **104**, 053108 (2021)

Editors' Suggestion   Featured in Physics

Using graphene conductors to enhance the functionality of atom chips

K. Wongcharoenbhorn,[1] R. Crawford,[1] N. Welch,[1] F. Wang,[1] G. Sinuco-León,[1,2] P. Krüger,[1,3] F. Intravaia,[1,4] C. Koller,[1,5] and T. M. Fromhold[1]

[1]*School of Physics and Astronomy, University of Nottingham, Nottingham NG7 2RD, United Kingdom*
[2]*Department of Chemistry, Durham University, South Road, Durham DH1 3LE, United Kingdom*
[3]*Department of Physics and Astronomy, University of Sussex, Brighton BN1 9QH, United Kingdom*
[4]*Humboldt-Universität zu Berlin, Institut für Physik, AG Theoretische Optik & Photonik, 12489 Berlin, Germany*
[5]*University of Applied Sciences Wiener Neustadt, Johannes Gutenberg-Straße 3, 2700 Wiener Neustadt, Austria*

(Received 7 May 2021; accepted 27 September 2021; published 16 November 2021)

We show that the performance and functionality of atom chips can be transformed by using graphene-based van der Waals heterostructures to overcome present limitations on the lifetime of the trapped atom cloud and on its proximity to the chip surface. Our analysis involves Green's-function calculations of the thermal (Johnson) noise and Casimir-Polder atom-surface attraction produced by the atom chip. This enables us to determine the lifetime limitations produced by spin flip, tunneling, and three-body collisional losses. Compared with atom chips that use thick metallic conductors and substrates, atom-chip structures based on two-dimensional materials reduce the minimum attainable atom-surface separation to a few hundred nanometers and increase the lifetimes of the trapped atom clouds by orders of magnitude so that they are limited only by the quality of the background vacuum. We predict that atom chips with two-dimensional conductors will also reduce spatial fluctuations in the trapping potential originating from imperfections in the conductor patterns. These advantages will enhance the performance of atom chips for quantum sensing applications and for fundamental studies of complex quantum systems.

DOI: 10.1103/PhysRevA.104.053108

I. INTRODUCTION

Cold-atom systems play a key role in both fundamental and applied aspects of quantum sensing as they provide a well-isolated and controllable platform while still being sensitive to fundamentally interesting interactions such as gravity or magnetic fields [1,2]. The high levels of uniformity and homogeneity of cold atomic ensembles also provide a platform for high-accuracy time standards [3,4]. Recent experiments have demonstrated atomic quantum sensors in precision accelerometers [5], in clocks [6], and in measuring magnetic fields with an unprecedented combination of high sensitivity (nanotesla), spatial resolution (microns), and field of view (approximately 100 μm) [7–14]. As a result, there is now worldwide activity on the development of cold-atom-based quantum sensing and timing technologies [15,16].

Miniaturizing and integrating cold-atom quantum systems for fundamental experiments and technology development have advanced through the creation of atom chips, which use microfabricated current-carrying wires to trap and control the atoms in an ultrahigh vacuum, typically 1–100 μm from the chip surface. Such chips enable coherent manipulation of the atoms' internal and external degrees of freedom [17,18], leading, for example, to on-chip formation of Bose-Einstein condensates (BECs) [19,20], atom interferometers [21,22], and interfacing quantum gases with nanomechanical oscillators [23], carbon nanotubes [24,25], and cryogenic surfaces [26–31]. However, commonly used metal wires with a typical thickness of approximately 1 μm, mounted on bulk insulating substrates, have adverse effects when trapped atom clouds approach the surface. Spatial imperfections in the wires roughen the trapping potential, Johnson noise currents induce spin-flip transitions that eject atoms from the trap, and the strong Casimir-Polder (CP) attraction between the atoms and the chip produce tunneling losses. Together, these loss mechanisms prevent the formation of long-lived microtraps at distances closer than several microns from the chip surface [32,33].

Overcoming these limitations is needed to advance both the fundamental and technological applications of micro- and nanoengineered environments for cold atoms. Trapping atoms closer to the chip offers a number of advantages. Higher magnetic field gradients and trap frequencies can be attained for a given current, thereby facilitating fast initial cooling, i.e., before three-body collisions become relevant, as required for creating BECs under less stringent vacuum requirements. Higher trapping frequencies also produce atomic gases that are closer to the one-dimensional (1D) limit and are thus better for studying the thermodynamics of low-dimensional gases. Submicron trapping has been realized by utilizing the balancing of attractive and repelling forces of light in nanofibers [34,35] and in ferromagnetic traps [36], but has proven difficult to achieve using current-carrying chip structures [37]. Anisotropic conductors have been suggested as a way to reduce Johnson noise and consequently atom-surface separations [38], as required for creating hybrid quantum devices comprising coherently coupled atomic and solid-state elements [39,40].

Achieving long lifetimes for atom clouds trapped within 1 μm of the chip surface will enable quantum gases to be controlled and addressed by potential landscapes whose spatial features are finer than the intrinsic length scales of atomic gases, for example, the healing length. Reducing atom-surface trapping distances will also advance chip-based sensors including the BEC microscope, which can image current flow patterns in planar conductors with a spatial resolution limited primarily by the distance of the BEC from the conductor [7–9,11,12,14].

The key advantage of using trapping wires made from graphene, or other two-dimensional conductors, is their lower level of Johnson noise [41,42]. This low Johnson noise originates from the orders-of-magnitude lower sheet electron density in graphene (and other 2D conductors) compared with metals, which dominates over the tendency of the higher carrier mobility in 2D materials to increase current fluctuations. We analyze and quantify this advantage in detail in Sec. III and Appendix A 2.

Here we show that atom chips containing two-dimensional conductors can in principle overcome the present limitations on the atom-surface separation and lifetime of the trapped atom cloud. Such trapping structures can be fabricated using, for example, graphene membranes that are either free standing or enclosed by two-dimensional insulating layers so as to form a van der Waals heterostructure [43,44]. This opens a route to achieving submicron trapping distances and hence fine features in the trapping potential landscape that are not attainable when conventional metallic wires are used. We demonstrate that van der Waals heterostructures can be used to form traps just a few hundred nanometers from their surface while maintaining trap lifetimes of at least 10 s. This exceeds the duration of most experiments on the atom clouds and of typical active operation cycles in cold-atom quantum sensors. In previous work on the possible use of two-dimensional electron gases as conductors in atom chips [41,42], the lifetime of nearby atomic gases was estimated by extrapolating from the rates of tunneling losses and Johnson-noise-induced spin flips near metallic conductors [42]. Here we present detailed calculations of the atom-cloud lifetimes, in which the same Green's-function formalism is used to determine both the CP potential and Johnson noise lifetimes, thereby ensuring a fully consistent picture of atom-loss rates.

The paper is organized as follows. In Sec. II we consider how atom-chip architecture and material composition affect the lifetime and minimum practical atom-surface separation of trapped atom clouds. In Sec. III we compare the limiting factors, specifically atom-cloud lifetime and spatial roughness, for traps formed less than 1 μm away from the surface of chips containing graphene or 1-μm-thick metallic trapping wires. Specifically, we present detailed calculations that quantify how two-dimensional conductors such as graphene can reduce the spin-flip atom losses resulting from Johnson noise in the conductor, as well as the tunneling losses due to CP atom-surface attraction, sufficiently to enable stable submicron trapping with atom-cloud lifetimes greater than 10 s. In Sec. IV we propose specific routes to the realization of graphene-based atom chips that operate under realistic experimental conditions. In Sec. V we conclude with an overview of possible further device geometries and experiments to demonstrate the performance and versatility of graphene-based atom chips. Further details of the calculations are given in the Appendixes.

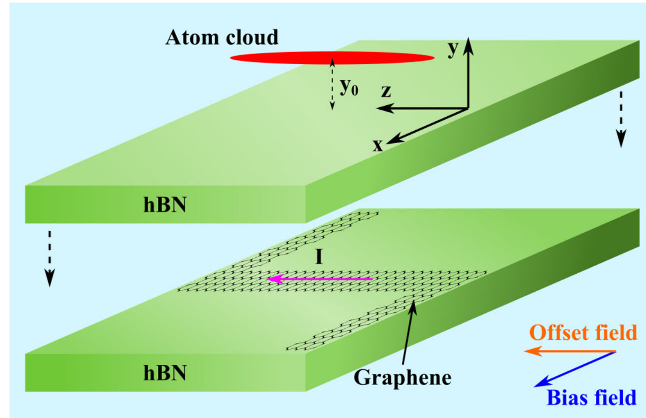

FIG. 1. Schematic diagram of the proposed graphene-based atom chip showing the Z-shaped graphene conducting channel (hexagonal graphene lattice pattern) carrying current I (pink arrow), encased by thin, protective, hBN cladding layers (upper and lower green slabs). The orientations of the applied magnetic bias field and the offset field are shown by blue and orange arrows, respectively. These fields combine with that produced by the conducting channel (current I) to trap a nearby atomic BEC (red).

II. PROPOSED ATOM-CHIP STRUCTURE

Henceforth, we consider microfabricated atom-chip structures that produce magnetic traps for clouds of ^{87}Rb atoms, as this approach will facilitate comparison to previous experiments. The implications for other species of alkali-metal atoms are straightforward to derive and do not differ qualitatively from the ^{87}Rb case. Our proposed graphene-based atom chip is shown schematically in Fig. 1. The chip comprises a Z-shaped graphene wire encased by two cladding layers of 10-nm-thick hexagonal boron nitride (hBN). Electrical current I through the Z-shaped wire generates an inhomogeneous magnetic field, which is supplemented by a constant applied bias field $\mathbf{B}_b$ and an offset (Ioffe) field $\mathbf{B}_0$ to create a magnetic field minimum at $\mathbf{r}_0 = (x_0, y_0, z_0)$. An ultracold atom cloud is trapped near this magnetic field minimum, whose value is nonzero due to the offset field, which suppresses atom losses due to Majorana spin-flip transitions [17]. The potential energy U_{mag} of the trapped atoms equals the interaction energy between the atomic magnetic moment $\boldsymbol{\mu}$ and the net magnetic field $\mathbf{B}(\mathbf{r})$, where $\mathbf{r}$ is the spatial position with respect to the coordinate origin, i.e.,

$$U_{\mathrm{mag}}(\mathbf{r}) = -\boldsymbol{\mu} \cdot \mathbf{B}(\mathbf{r}) = m_F \mu_B g_F |\mathbf{B}(\mathbf{r})|. \tag{1}$$

Here μ_B is the Bohr magneton and g_F is the Landé factor of the relevant hyperfine state. For the ^{87}Rb atoms considered here, this is typically the $|F, m_F\rangle = |2, 2\rangle$ level of the $5\,^2S_{1/2}$ ground state. Provided the magnetic quantum number m_F is a good quantum number, atoms in metastable low-field seeking states, whose magnetic moment is aligned antiparallel to the magnetic field orientation, will be trapped near the magnetic field minimum $\mathbf{r}_0$, where U_{mag} is also minimal.

The interplay between three energy scales determines the lifetime of the trapped atomic gas. The first energy scale is the trap depth given by $V_0 = |\boldsymbol{\mu} \cdot \Delta\mathbf{B}|$, where $\Delta\mathbf{B}$ is the difference between the maximum and the minimum values of the magnetic field. The second scale is the thermal energy $k_B T_{\text{cloud}}$ related to the temperature T_{cloud} of the trapped atoms, where k_B is the Boltzmann constant. The last energy scale is the ground-state energy of the trapped atoms E_0. Provided a sufficiently deep magnetic trap, i.e., $V_0 \gg k_B T_{\text{cloud}}, E_0$ is located far away from any surface, the overall lifetime of the trapped atoms is limited by collisions with the background gas. In typical atom-chip experiments, pressures of 10^{-10}–10^{-11} mbar or below can be reached, for which the background pressure-limited lifetime of the trapped atoms is of the order of tens of seconds or better [17]. As the atom cloud approaches the chip surface, its lifetime is reduced by modification of the trapping potential due to CP interactions with the surface (see Figs. 7 and 8 in Appendix A) and Johnson noise in the conductor, which can cause the atoms to undergo spin-flip transitions into untrapped states. Lower-frequency Johnson noise, comparable to the trap frequencies, can also potentially cause atom losses due to parametric heating of the atom cloud. However, the rates of such heating are orders of magnitude lower than the spin-flip loss rates [32]. Due to the low Johnson noise and CP potential near graphene-based atom chips, the lifetime of atom clouds trapped near such chips will, beyond a certain trapping distance, be limited only by the background pressure as we quantify below.

As the atom-surface trapping distance decreases, the trap frequencies must be increased in order to reduce depletion by the CP interaction. In turn, this increases the density of the trapped atom cloud and therefore also increases the rate of three-body collision losses discussed in Sec. III. In order to determine the optimal trapping distance, the interplay of three-body losses, the minimum detection density of the atom cloud, and the CP interaction all have to be considered, as discussed in Sec. III.

III. LIFETIME OF A TRAPPED ATOMIC BEC

In this section we find an analytical expression for the total loss rate of an elongated atomic BEC trapped in the vicinity of an atom chip. We consider contributions from atom tunneling towards the chip surface, Johnson-noise-induced losses, and the three-body loss mechanism. Details of the loss rate calculations are given in the Appendixes.

A. Methodology

First, we consider a harmonic magnetic trapping field $\mathbf{B}(\mathbf{r})$, formed near the surface of an atom chip in the coordinate system shown in Fig. 1, where $\mathbf{r} = (x, y, z)$; ω_x, ω_y, and ω_z are the characteristic trapping frequencies in the x, y, and z axes, respectively; and the trap center is located at $\mathbf{r}_c = (0, y_c, 0)$. Regarding the interaction between the atom and the electromagnetic field, we take the 2D layers of the atom chip to have infinite lateral extent, which is a good approximation for the short atom-surface separations that are our focus here.

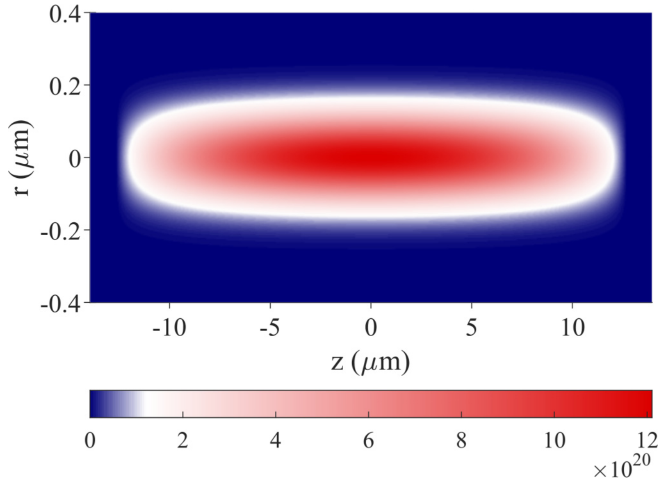

FIG. 2. Colormap of the atom volume density calculated for the trapped atom cloud using the Thomas-Fermi distribution in Eq. (4). The color bar scale is in units of m^{-3}. The parameters are $\omega_r = 2\pi \times 20$ kHz, $\omega_z = 0.006 \times \omega_r$, and $N = 750$.

The potential energy profile of an atom interacting with this magnetic field is modeled by an anisotropic three-dimensional harmonic-oscillator potential

$$U(x, y, z) = \tfrac{1}{2} m \left[\omega_x^2 x^2 + \omega_y^2 (y - y_c)^2 + \omega_z^2 z^2\right]. \quad (2)$$

Note that this magnetic potential originates from the interaction of the magnetic moment of the trapped atom and the magnetic field given in Eq. (1) and that the actual potential profile of an atom-chip trap is determined by the wire and current configurations. Equation (2) gives a good approximation for the potential landscape generated by the Z-shaped trapping wires often used in atom-chip experiments.

We assume that such a magnetic trap has cylindrical symmetry and is elongated along the z axis so that $\omega_r = \omega_{x,y}$ and $\omega_r \gg \omega_z$, where ω_r denotes the trapping frequency in the radial direction (i.e., in the x-y plane). We also assume that ω_r is so high that the trapped atoms only occupy the ground-state energy in the radial direction. To include the perturbing effect of the CP potential on the effective trapping frequency in the y direction, ω_{eff}, henceforth we approximate the radial trapping frequency as $\omega_r = \sqrt{\omega_x \omega_{\text{eff}}}$. An additional offset magnetic field $\mathbf{B}_0 = (0, 0, B_z)$, of order millitesla, is added in the z direction to ensure that the magnetic field is nonzero at the trap center. Together, these assumptions enable us to treat the magnetic potential energy landscape as a highly elongated quasi-one-dimensional trap.

It follows from the above assumptions about the trapping frequencies that the chemical potential μ of the condensate must satisfy the constraints

$$5\hbar\omega_z < \mu < \tfrac{3}{2}\hbar\omega_r, \quad (3)$$

which allows us to further assume that the mean atom density profile of the condensate can be described by a one-dimensional Thomas-Fermi distribution in the elongated (z) direction and by the Gaussian ground-state wave function of a quantum harmonic oscillator in the tightly confining radial (r) direction [45]. The atom density profile is then given by

(see Fig. 2)

$$\rho_0(r,z) = \frac{1}{U_0}\left(\mu_{\text{eff}} - \frac{m\omega_z^2}{2}z^2\right)e^{-r^2/2a_r^2}, \tag{4}$$

where $U_0 = 4\pi\hbar^2 a_T/m$ is the effective interaction strength for a pair of slowly moving atoms of s-wave scattering length a_T [46], $\mu_{\text{eff}} = \mu - \hbar\omega_r$, $m = 1.44 \times 10^{-25}$ kg is the mass of an ^{87}Rb atom, $r = \sqrt{x^2 + (y - y_c)^2}$ is the radial distance relative to the center of the trap, and $a_r = \sqrt{\hbar/m\omega_r}$ is the characteristic harmonic-oscillator length. The number of atoms N in the BEC follows by integrating $\rho_0(r,z)$ over all space. Integrating Eq. (4) over the radial coordinate gives the mean line density profile along the z axis (see the Appendixes for details)

$$n_0(z) = \frac{2\pi a_r^2}{U_0}\left(\mu_{\text{eff}} - \frac{m\omega_z^2}{2}z^2\right). \tag{5}$$

The chemical potential μ of the trapped atom cloud is determined by the peak mean line density, i.e., at $z = 0$, as [47]

$$\mu = [2a_T n_0(0) + 1]\hbar\omega_r, \tag{6}$$

where $a_T = 5.6$ nm is the scattering length for ^{87}Rb atoms in the $|F, m_F\rangle = |2, 2\rangle$ state [48].

We now define the total lifetime of the trapped atom cloud τ_{tot} to be the time taken for the initial peak atom line density $n_0(z = 0)$ to drop below the smallest experimentally detectable line density, which we take to be $n_{\min} = 3 \times 10^6$ m^{-1} [49]. We determine the upper limit of τ_{tot} by taking $n_0(z = 0)$ to be the maximum possible value $n_{\max} = 14.8 \times n_{\min}$ satisfying the inequality (3).

Let us now consider the density-dependent loss rates originating from three distinct atom-loss mechanisms: Johnson-noise-induced spin flips, quantum tunneling to the chip surface, and three-body processes. The Johnson-noise-induced loss rate is

$$\left.\frac{dn_0(z)}{dt}\right|_{\text{JN}} = -\Gamma_{\text{JN}} n_0(z), \tag{7}$$

where Γ_{JN} is the Johnson-noise-induced spin-flip transition rate given in Eq. (A13) in Appendix A. As described above, the tunneling loss rate has a similar form

$$\left.\frac{dn_0(z)}{dt}\right|_{\text{tun}} = -\Gamma_{\text{tun}} n_0(z), \tag{8}$$

where Γ_{tun} reflects the tunneling rate (see Appendix A). By contrast, the three-body loss rate is proportional to the cube of the mean line density [50,51]

$$\left.\frac{dn_0(z)}{dt}\right|_{\text{3b}} = -\Gamma_{\text{3b}} n_0(z)^3, \tag{9}$$

where $\Gamma_{\text{3b}} = \kappa_{\text{Rb}}/12\pi^2 a_r^4$ and $\kappa_{\text{Rb}} = 1.8 \times 10^{-41}$ m^6 s^{-1} determine the three-body recombination rate for ^{87}Rb in the $F = m_F = 2$ state [52]. Combining all three distinct loss rates gives the total loss rate

$$\left.\frac{dn_0(z)}{dt}\right|_{\text{tot}} = -\Gamma_{\text{3b}} n_0(z)^3 - (\Gamma_{\text{tun}} + \Gamma_{\text{JN}}) n_0(z). \tag{10}$$

In this paper we will only consider losses occurring at $z = 0$, where the line density peaks and so the total loss rate is maximal. Hence, we determine the lower limit on the total lifetime given by the integral

$$\tau_{\text{tot}} = \int_{n_{\max}}^{n_{\min}} \left.\frac{dn_0(z)}{-\Gamma_{\text{3b}} n_0(z)^3 - (\Gamma_{\text{tun}} + \Gamma_{\text{JN}}) n_0(z)}\right|_{z=0}, \tag{11}$$

which can be integrated analytically to yield

$$\tau_{\text{tot}} = \frac{\ln\left[\frac{\Gamma_{\text{3b}} n_{\min}^2 + (\Gamma_{\text{tun}} + \Gamma_{\text{JN}})}{\alpha^2 \Gamma_{\text{3b}} n_{\min}^2 + (\Gamma_{\text{tun}} + \Gamma_{\text{JN}})}\right] + 2\ln(\alpha)}{2(\Gamma_{\text{tun}} + \Gamma_{\text{JN}})}, \tag{12}$$

where $\alpha = n_{\max}/n_{\min} = 14.8$.

B. Results

In this section we calculate and compare atom-cloud lifetimes for three different surface structures: a 1-μm-thick gold slab, a graphene monolayer, and a graphene monolayer encased by two 10-nm-thick hBN layers. Results and comparisons with thinner gold wires are presented in Appendix A. The first structure is representative of the present generation of atom chips and provides typical lifetimes for comparison with graphene-based devices. The second structure is the theoretical limit for 2D materials and exemplifies the predicted improvements in performance and functionality. The third atom-chip structure is within the scope of existing fabrication techniques for van der Waals heterostructures [43,44]. The graphene conductor is encased within hBN multilayers, which support it and shield it from adsorbates. When trapping atoms close to a surface, especially metal, stray electric fields are produced from the polarization of adsorbed atoms [23]. Although this effect has not yet been measured for graphene surfaces, covering the graphene layer with a dielectric layer such as hBN is expected to suppress these effects by limiting polarization of any adsorbates and keeping them away from the graphene layer(s), so preventing them doping it.

Figure 3 shows the lifetimes resulting from each of the three loss mechanisms considered in the preceding section, together with the total lifetime, calculated versus the position of the harmonic trap center y_0 for ^{87}Rb atoms near a graphene monolayer [Fig. 3(a)] and the 1-μm-thick gold slab [Fig. 3(b)]. Note that in this figure and henceforth, all the lifetimes are calculated using Eqs. (7)–(12), which account for the minimum experimentally detectable atom density. The unperturbed transverse trapping frequency $\omega_y = 2\pi \times 20$ kHz is used in all cases. Curves are plotted over the range of y_0 values for which the total potential energy variation normal to the surface forms a trap (see Appendix A).

Considering Fig. 3, we first note that the three-body loss lifetimes (red dashed curves) are identical for the two structures, as expected from Eq. (9). Second, as a consequence of weaker CP attraction, the tunneling loss lifetime for the graphene monolayer is longer than for the gold slab (compare green dash-dotted curves) and the minimum atom-surface trapping distance is lower. Third, significant improvement in the Johnson-noise-limited lifetime is apparent for the graphene monolayer. Whereas Johnson noise in the metal wire limits the total atom lifetime, for graphene the three-body lifetime of approximately 12.5 s is the limiting factor and Johnson noise is insignificant. Physically, this is because the areal electron density in the graphene is approximately eight

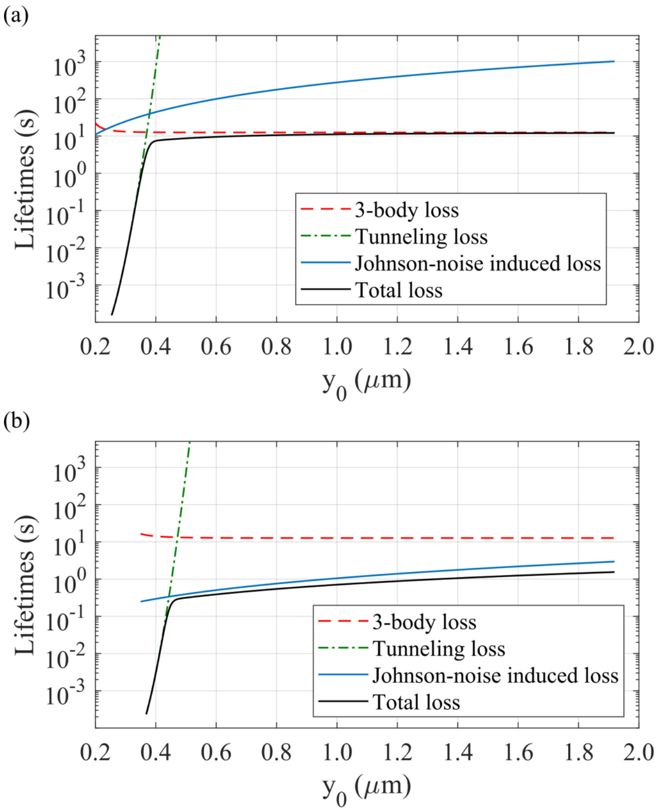

FIG. 3. Lifetimes calculated [from Eqs. (7)–(12)] versus the position of the harmonic trap center y_0 for an ^{87}Rb quasicondensate trapped near (a) a graphene monolayer and (b) a 1-μm-thick gold slab, for three different loss mechanisms: three-body processes (red dashed curves), tunneling losses (green dash-dotted curves), and Johnson-noise-induced losses (blue solid curves). The total lifetime is shown by the black solid curves. For the graphene monolayer, the total lifetime is limited by three-body losses to approximately 12.5 s, whereas for the gold slab the total lifetime is limited by Johnson noise. The other parameter is $\omega_y = 2\pi \times 20$ kHz.

orders of magnitude lower than in the metal wire, whereas the mobility is only approximately four orders of magnitude higher in graphene. Consequently, the Johnson noise produced by the graphene is approximately four orders of magnitude lower than for the metal wire. Further explanation and detailed analysis of the lower Johnson noise produced by graphene compared with the metal wire is given in Appendix A 2.

Figure 4 shows lifetimes calculated for ^{87}Rb atoms near the hBN-graphene heterostructure, taking the same trapping frequency as in Fig. 3. The only noticeable difference in the lifetimes compared with those for a graphene monolayer alone relates to tunneling loss (green dash-dotted curve). For given y_0, the hBN-graphene structure generates a higher CP potential and hence a shorter tunneling lifetime and a higher minimum distance from the trap center to the surface (see Appendix A). The Johnson noise is insensitive to the addition of the hBN cladding layers because such layers change neither the number nor mobility of the free charge carriers in the graphene and the total lifetime is still limited by the three-body loss mechanism.

We have also made a preliminary analysis of the effect of the surface temperature T on the total lifetime of the

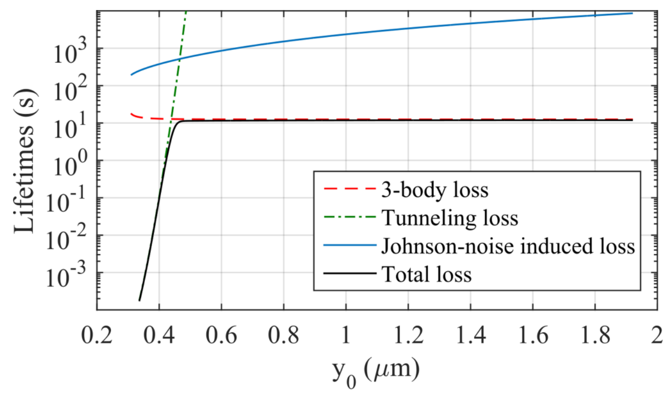

FIG. 4. Lifetimes calculated [from Eqs. (7)–(12)] versus the position of the harmonic trap center y_0 for an ^{87}Rb quasicondensate trapped near an hBN-encased graphene heterostructure for three different loss mechanisms: three-body processes (red dashed curve), tunneling losses (green dash-dotted curve), and Johnson-noise-induced losses (blue solid curve). The total lifetime is shown by the black solid curve. For $y_0 > 0.5$ μm, where the magnetic trap has a well-defined barrier on the side near the surface, the lifetimes are virtually identical to those for a single layer of graphene. The parameters are $\omega_y = 2\pi \times 20$ kHz and hBN thickness equal to 10 nm.

atom cloud. Figure 5 indicates that, for the gold slab (solid curves), the lifetime increases several fold as T decreases from 300 K to 50 K when $y_0 \gtrsim 0.4$ μm probably because the mean thermal photon occupation number decreases (see Appendix A). By contrast, for the graphene-hBN heterostructure (dashed curves), the lifetime barely changes with temperature for atom-surface separations in this regime. Note that, even when $T = 50$ K, the lifetimes calculated for the graphene-hBN heterostructure are still several times longer than those for the gold slab. Further work is required to investigate the temperature dependence in more detail.

Figure 6 shows colormaps of the total lifetimes, calculated versus the position of the trap center from the surface

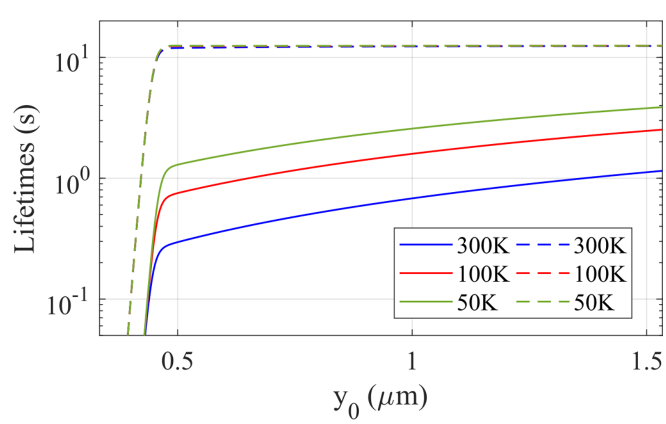

FIG. 5. Lifetimes calculated [from Eqs. (7)–(12)] versus the position of the harmonic trap center y_0 for an ^{87}Rb quasicondensate trapped near a 1-μm-thick gold slab (solid curves) and an hBN-encased graphene heterostructure (dashed curves) for surface temperatures $T = 50$ K (green curves), 100 K (red curves), and 300 K (blue curves). Lifetimes of atom clouds near the gold slab increase as T decreases, but are lower than for the heterostructure. The other parameter is $\omega_y = 2\pi \times 20$ kHz.

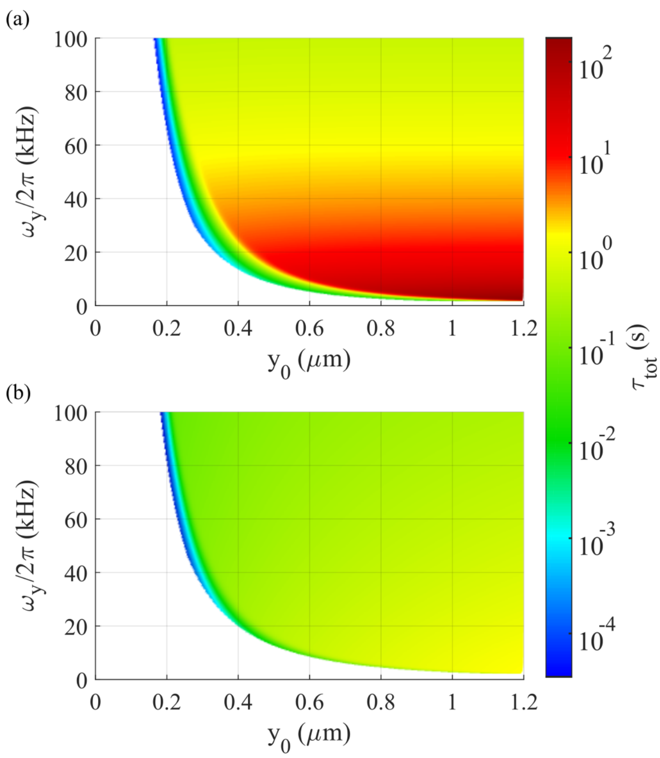

FIG. 6. Colormaps of total lifetimes, calculated [from Eqs. (7)–(12)] versus y_0 and $\omega_y/2\pi$ for (a) an hBN-encased graphene heterostructure and (b) a 1-μm-thick gold slab with a common color scale (right). The lifetime is not defined in the white region because the CP potential distorts the harmonic magnetic potential (i.e., reduces the barrier nearest to the surface) so strongly that the trap cannot be formed. For any given y_0 and $\omega_y/2\pi$ values, the lifetime for the hBN-graphene structure is longer than for the thin gold slab.

and the transverse trapping frequency for the hBN-graphene heterostructure [Fig. 6(a)] and the 1-μm-thick gold slab [Fig. 6(b)]. The color scale is logarithmic and is applicable to Figs. 6(a) and 6(b). Whereas the total lifetime for the thin gold slab is mainly below 1 s (yellow-green in color scale), for the hBN-graphene structure it exceeds 100 s (red shading) for high-y_0 and low-ω_y values.

IV. POSSIBLE IMPLEMENTATIONS

In order to see whether a closed surface magnetic trap can be realized using graphene wires, we assume a simple side guide configuration, consisting of a graphene wire carrying a current I and a bias magnetic field of magnitude $|\mathbf{B}_b|$. This will form a magnetic minimum at a distance

$$y_0 = \frac{\mu_0}{2\pi}\frac{I}{|\mathbf{B}_b|} \tag{13}$$

from the graphene sheet. Using the derivation given in [17] and assuming that the trapping distance is larger than the width of the graphene wire, the trapping frequency is approximated by

$$\omega_y = 2\pi\sqrt{\frac{\mu_B g_F m_F}{m|\mathbf{B}_0|}\frac{|\mathbf{B}_b|^2}{\mu_0 I}}, \tag{14}$$

where $|\mathbf{B}_0|$ is the magnitude of the offset magnetic field parallel to the direction of current flow used to avoid Majorana spin flips. A trap frequency of $\omega_y \approx 2\pi \times 20$ kHz is therefore realizable at a distance of 400 nm with a total current of 0.7 μA in addition to a bias field of 35 μT and an offset (Ioffe) field of 80 μT. Since exfoliated and epitaxial graphene on bulk substrates can support current densities in excess of approximately 1000 A/m even in an ultrahigh vacuum [53,54] and current densities as high as approximately 700 A/m have been reported for free-standing monolayer graphene [55], a graphene conducting channel only 50 nm wide would be sufficient to ensure trap operation with negligible heating. Note that such a narrow wire would reduce the Johnson noise below the values calculated here for an infinitely extended graphene sheet. Wires with larger widths could increase the possible trapping frequencies or enable trapping further from the surface, which may assist with loading the trap. We note, however, that such a trap could not be loaded directly but would need to be mounted on a carrier chip featuring thick metal wires, which generate the field used initially to cool and trap the atoms. This carrier chip must be placed far enough from the graphene and the atoms to produce negligible Johnson noise and CP attraction effects, but also close enough to create a sufficiently compressed trap. Given a 50-μm separation between the atom cloud and the carrier chip, gold wires carrying a current of 1 A could produce the transverse trap frequency of $\omega_r = 2\pi \times 20$ kHz needed for the traps shown in Figs. 3, 4, and 5. Since thin van der Waals heterostructures are almost transparent, laser light can pass through them and be retroreflected from a metal coating on the carrier chip in order to form a mirror magneto-optical trap. Here we note that thin hBN is more (less) reflective than a 290-nm-thick SiO_2 wafer at wavelengths above (below) 530 nm and that the contrast increases proportionally to the number of hBN layers [56].

In an alternative configuration, the potential for trapping the atoms could be provided by optical fields, for example, an electromagnetic standing wave generated by on-chip mounted optics. In this case, the graphene wires could be used to perturb strongly the optical potential or act as a source of magnetic fields to enable, for example, tuning the scattering length via Feshbach resonances.

Graphene-based atoms chips could be fabricated by molecular-beam epitaxy growth of graphene [57–59] or deposition of exfoliated graphene on hBN, followed by selective etching of the graphene to define the conducting channel and finally deposition of capping layers of hBN either by epitaxial growth or by placing exfoliated hBN layers, as now widely done to create van der Waals heterostructures [43,44]. Such structures could be placed over deep (~50-μm) trenches etched into a silicon wafer on which gold control wires are deposited to assist with the trapping procedure. This approach would be compatible with further component integration such as on-chip optical waveguides, sensing devices, and quantum dots.

V. CONCLUSION

In summary, we have presented a general formalism for calculating how the lifetime of an atomic quantum gas is affected by the Johnson noise and atom-surface CP attraction of van der Waals heterostructures comprising arbitrary configurations of 2D materials such as graphene. The electromagnetic reflection coefficients and corresponding electrical conductivities of the 2D layers are of crucial importance in determining both the Johnson noise and CP potential. Since both of these parameters are lower for graphene than for the metal layers generally used in atom chips, so too are the Johnson noise and CP atom-surface attraction. Consequently, for given atom-surface separation, the spin-flip and tunneling loss rates are both lower near graphene-based van der Waals heterostructures than near metal wires, meaning that such heterostructures can improve the performance of atom chips. For example, although high Johnson noise limits the lifetime of atom clouds trapped between 0.4 and 2 μm from a metal wire to less than 1 s, such noise is negligible for atoms trapped near graphene, whose lifetime can in principle reach approximately 100 s, limited only by three-body losses and background gas collisions. For atom-surface separations below 0.4 μm, the lifetime of the atom cloud is limited by tunneling losses for both metallic and 2D conductors. However, due to the weak CP atom-surface attraction, such losses are lower near van der Waals heterostructures and around four orders of magnitude lower for atoms held 0.4 μm from the surface.

As a result of their favorable noise and CP characteristics, van der Waals heterostructures offer a solid-state solution to the long-standing challenge of holding ultracold-atom clouds closer than 1 μm from an atom-chip surface for long enough (up to 100 s) to perform various experiments and measurements on the atom cloud. Moreover, van der Waals heterostructures that enable robust submicron atom trapping would control atomic condensates on length scales that are smaller than presently achievable optically and below the healing length, thereby providing access to new regimes of quantum many-body physics. The ability to achieve long lifetimes for ultracold atoms held as close as 400 nm to an electronic device might also open a route to creating new hybrid atomic–solid-state quantum systems, for example, a Rydberg atom coupled to a quantum dot formed within a 2D conductor [60,61]. Since the micron-scale confinement length of electrons in the quantum dot is similar to that of the excited electron in the Rydberg atom, new types of electron orbital, shared between the atom and the condensed matter parts of the system, may be created. Such hybrid states may yield new regimes of quantum control and information storage or processing, for example, relating to sideband cooling of graphene [62]. Realizing such devices will however be highly challenging and require significant experimental, device fabrication, and technical advances. We hope that our work will stimulate the follow-on research required to identify and overcome these challenges.

APPENDIX A: INFLUENCE OF THE ATOM CHIP ON TRAPPED ATOMS

1. CP potential and resulting atom tunneling towards the chip surface

The Casimir-Polder potential is essentially a position-dependent shift of the atomic energy level structure, induced by the interaction of the atom with the surrounding surface-modified electromagnetic radiation [63,64]. In general, the presence of an object modifies a system's electromagnetic density of states, due to the boundary conditions that the field has to satisfy on the surface of the object. The extent of the modification, and therefore the strength of the CP potential, depends on the object's specific position in space, on its form, and on the material(s) from which it is made, in particular the layer composition, shown schematically in Fig. 7.

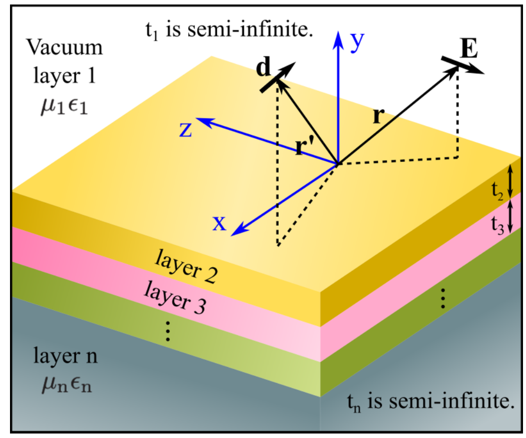

FIG. 7. Schematic diagram of a dipole (electric in the case of our CP potential calculation but magnetic for our Johnson-noise analysis) near an n-layer system, where each layer is designated by index $l = 1, 2, \ldots, n$. Each layer is characterized by thickness t_l, permeability μ_l, and permittivity ϵ_l. The top surface of upper material layer 2 (yellow) coincides with the origin of the y coordinate. The dipole (depicted by the arrow labeled **d**) is located at $\mathbf{r}' = (x', y', z')$ in layer 1, above the solid material layers, and acts as a point source. The arrow labeled **E** represents the orientation of the electric field of frequency ω at point **r**, which is related to the dipole **d** via a total Green's tensor. Note also that t_1 and t_n are infinite, corresponding to semi-infinite top and bottom layers.

Generally, an atom experiences an attractive CP force towards metallic and dielectric surfaces (Fig. 8). In atom-chip

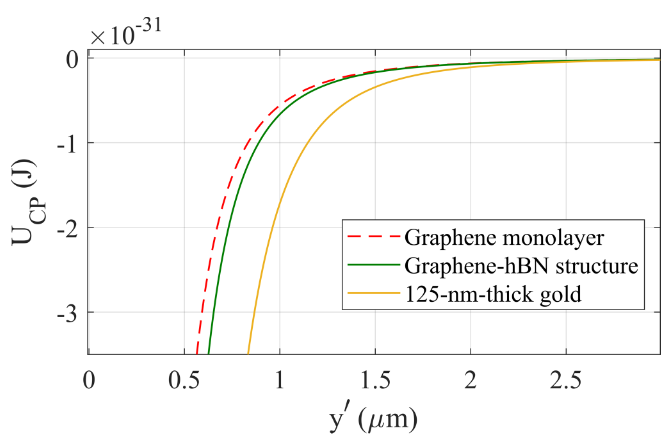

FIG. 8. CP potential $U_{\rm CP}$ calculated versus the position y' of an ^{87}Rb atom from the surface of a graphene monolayer (red dashed curve), a heterostructure comprising a graphene monolayer encased by two 10-nm-thick hBN layers (green solid curve), and a 125-nm-thick gold slab (yellow solid curve) at temperature $T = 300$ K.

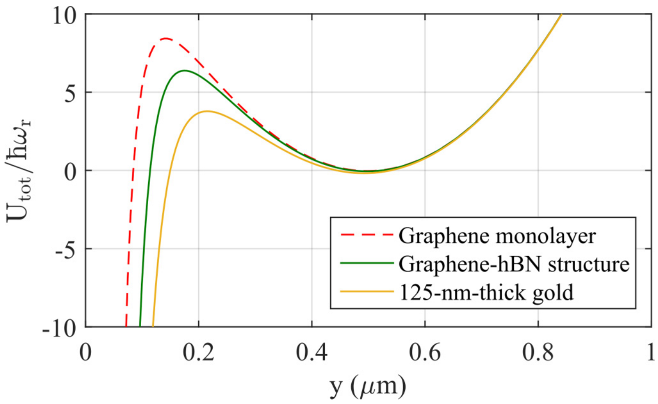

FIG. 9. Total potential U_{tot} calculated versus distance y of an ^{87}Rb atom from the surface of a free-standing graphene monolayer (red dashed curve), a graphene monolayer encased on each side by a 10-nm-thick hBN sheet (green solid curve), and a 125-nm-thick gold sheet (yellow solid curve). The total potential is the sum of the CP potential and the harmonic model trapping potential, which is centered at $y = 0.5$ μm with radial trapping frequency $\omega_r = 2\pi \times 20$ kHz. All curves are for $T = 300$ K.

systems this behavior effectively lowers the barrier at the side of a magnetic trap that is nearest the surface, as shown in Fig. 9. In turn, this enables atoms to tunnel out of the trap and be lost from the atom cloud. Tunneling losses induced by the CP potential affect key atom-chip performance parameters such as the integration time for sensor applications and the coherence time for quantum memories. In the present generation of atom chips, metal wires used to generate the magnetic field lead to a large CP attraction on trapped atoms located within approximately 1 μm of the surface. This imposes a minimum trapping distance of 10–100 μm for typical atom-chip experiments [17,65,66]. Our proposed 2D material-based atom chips are expected to exert very low CP attraction, due to their extremely small (less than 100 nm) thickness and their specific material properties, thereby opening a different route to entering the submicron atom-surface trapping regime.

For a system in equilibrium at a temperature T consisting of an atom located at position $\mathbf{r}'$ from a nearby material body (see Fig. 7), both interacting with the electromagnetic field, the CP potential is given by [67,68]

$$U_{\mathrm{CP}}(\mathbf{r}') = \mu_0 k_B T \sum_{j=0}^{\infty}{}' \xi_j^2 \alpha(i\xi_j) \mathrm{tr}[\mathbf{G}^{(1)}(\mathbf{r}', \mathbf{r}', i\xi_j)], \quad \text{(A1)}$$

where μ_0 is the permeability of vacuum, $\hbar$ is the reduced Planck constant, $\alpha(\omega)$ is the atomic polarizability, and $\xi_j = 2\pi k_B T j/\hbar$ is commonly known as the Matsubara frequency [69]. The prime on the Matsubara sum in Eq. (A1) indicates that the $j = 0$ term carries half weight [68]. In Eq. (A1), $\mathbf{G}^{(1)}(\mathbf{r}', \mathbf{r}', \omega)$ is the scattering Green's tensor, which contains the information about the material's optical properties and the geometry of the system.

For atom-surface separations shorter than the size of the components of an actual atom chip (typically of the order of a few tens of microns or larger) we can consider that the atoms are interacting with a large layered surface. In this case the expression for the Green's tensor is known and we present it explicitly in Appendix B. As shown there, in order to determine the expression of the Green's tensor we need to evaluate the reflection coefficients of the electromagnetic field incident on the atom-chip structure. In our case, the multilayer configurations allow their determination using the scattering or the transfer-matrix approach [70,71] in combination with models describing the optical properties of graphene, hBN, and gold (see Appendix C for details). In this work we take the Fermi energy and electron relaxation rate of graphene to be $E_F = 0.1$ eV and $\gamma = 4$ THz, respectively, corresponding to typical values found both theoretically [72–75] and in experiments [76].

In this paper we consider a simple model of alkali-metal atoms with atomic polarizability of the form [68,77]

$$\alpha(i\xi_j) = \alpha_0 \frac{\omega_{\mathrm{T}}^2}{\omega_{\mathrm{T}}^2 + \xi_j^2}, \quad \text{(A2)}$$

where α_0 is the ground-state static polarizability and ω_{T} is the frequency of the dominant atomic transition. In the case of ^{87}Rb atoms, $\alpha_0 = 5.27 \times 10^{-39}$ F m^2 [78] and $\omega_{\mathrm{T}} = 2\pi \times 384$ THz is the $D2$ line transition frequency corresponding to a wavelength of 780 nm [79].

Equation (A1) is sufficiently generic to enable the CP potential to be calculated for our atom-chip system and compared consistently with other materials and structures. In Fig. 8 we compare the CP potential U_{CP} calculated versus the separation y' of an ^{87}Rb atom from three different material systems: a graphene monolayer (red dashed curve) for which CP potential calculations have been reported previously [77,80–85], a heterostructure comprising a graphene monolayer encased by two 10-nm-thick hBN layers (green solid curve), and a 125-nm-thick gold slab (yellow solid curve), all at $T = 300$ K. We choose the thickness of the gold slab to be 125 nm because this is among the smallest reported thicknesses at which gold wires in atom-chip experiments [86] have a conductivity that still behaves as bulk. Even in this limit of metallic conductor thickness, at $y' \approx 1$ μm, the CP potential for the heterostructure is approximately 40% of that for the thin gold slab.

The effect of the CP potential on the total trapping potential U_{tot} can be illustrated by modeling the magnetic trapping potential U_H as simple harmonic and adding the CP potential, giving

$$U_{\mathrm{tot}}(y) = U_{\mathrm{H}}(y) + U_{\mathrm{CP}}(y). \quad \text{(A3)}$$

The simple harmonic potential takes the form

$$U_{\mathrm{H}}(y) = \tfrac{1}{2} m\omega_r^2 (y - y_c)^2, \quad \text{(A4)}$$

where m is the mass of the trapped atom, ω_r is the radial trapping frequency, and y_c is the position of the center of the simple harmonic trap measured from the surface; note that y_c is not necessarily equal to the minimum of the total potential.

Figure 9 shows the resulting total trapping potential U_{tot} calculated versus distance y of an ^{87}Rb atom from a graphene monolayer (red dashed curve), an hBN-graphene monolayer-hBN heterostructure (green solid curve) and a 125-nm-thick gold slab (yellow solid curve) calculated taking [see Eq. (A4)] $\omega_r = 2\pi \times 20$ kHz, $y_c = 0.5$ μm, $T = 300$ K, and the mass of an ^{87}Rb atom $m = 1.44 \times 10^{-25}$ kg. It is apparent that the

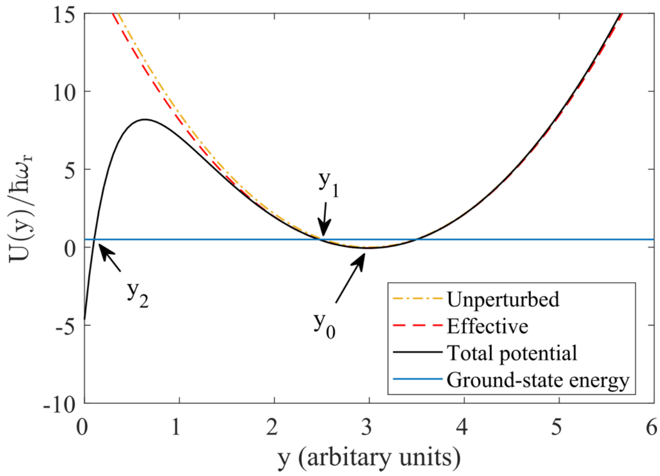

FIG. 10. Schematic diagram of the total trapping potential $U_{\rm tot}(y)$ (black solid curve) plotted versus distance y of an ^{87}Rb atom from an atom-chip surface. The blue solid line indicates the ground-state energy of the quantum harmonic oscillator $E = \hbar\omega_{\rm eff}/2$, where $\omega_{\rm eff}$ is the effective characteristic frequency of the simple harmonic trap (red dashed curve), which is perturbed by the CP potential, as described in the text, and approximates $U_{\rm tot}(y)$ near the minimum. The positions y_0, y_1, and y_2, indicated by arrows, are, respectively, the actual trap center and the two classical turning points for the left-hand potential energy barrier, where $U(y_1) - U(y_0) = U(y_2) - U(y_0) = \hbar\omega_{\rm eff}/2$. The yellow dash-dotted curve is the potential of the unperturbed simple harmonic trap.

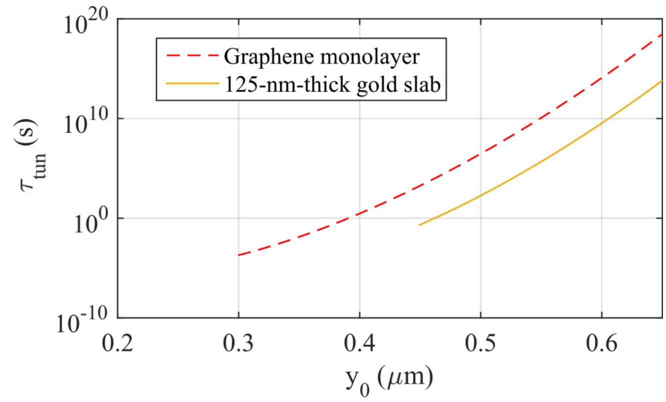

FIG. 11. Tunneling lifetime $\tau_{\rm tun}$ calculated versus the position of the harmonic trap center y_0 for an ^{87}Rb atom trapped near a graphene monolayer (red dashed curve) and a 125-nm-thick gold slab (yellow solid curve). The weaker CP attraction for graphene gives rise to a higher, wider tunnel barrier and consequently a higher tunneling lifetime. The parameters are $T = 300$ K and $\omega_r = 2\pi \times 20$ kHz.

CP potential distorts the simple harmonic trap: An energy barrier of finite height and width appears near the surface for $y < y_c$. The height and width effectively scale with the distance of the trap center from the surface, thereby giving rise to tunneling losses, which deplete the trapped atom cloud. Since graphene creates a weaker CP attraction than even the thin gold conductor, the tunneling loss rates for graphene-based atom chips are lower than for conventional atom chips and we quantify this benefit below. Consequently, graphene-based atom chips offer a performance advantage over the present generation of atom chips, which use metallic conductors as current-carrying wires.

In order to estimate the tunneling loss rate $\Gamma_{\rm tun}$ of an atom cloud trapped in the finite potential well shown schematically by the black solid curve in Fig. 10, we employ Gamow's theory of α decay [87]. In this model, the atom is considered to oscillate inside the potential well and can escape by tunneling through the finite barrier nearest the surface each time it is incident on that barrier. The tunneling rate is determined by the frequency at which the atom approaches the barrier f and the transmission probability $\tilde{T}$ that the atom tunnels out at each attempt. Mathematically, we have

$$\Gamma_{\rm tun} = f \times \tilde{T}. \tag{A5}$$

Figure 10 shows that the deformation of the unperturbed harmonic magnetic potential (yellow dash-dotted curve) by the CP interaction also yields an effective perturbed harmonic potential (red dashed curve) with a lower trapping frequency, $\omega_{\rm eff}$, and whose minimum shifts from $y = y_c$ to a new position y_0. The perturbed harmonic potential therefore takes the form

$$U_{\rm eff}(y) = \tfrac{1}{2} m\omega_{\rm eff}^2 (y - y_0)^2, \tag{A6}$$

where a Taylor expansion of $U_{\rm tot}(y)$ about $y = y_0$ yields

$$y_0 \approx y_c + \frac{U'_{\rm CP}(y_c)}{m\omega_r^2}, \quad \omega_{\rm eff}^2 \approx \omega_r^2 + U''_{\rm CP}(y_0). \tag{A7}$$

Atoms in the ground state of this effective potential have an energy $E = \hbar\omega_{\rm eff}/2$ and approach the barrier at frequency $f = \omega_{\rm eff}/2\pi$. Using the Wentzel-Kramers-Brillouin approximation, the transmission probability through the tunnel barrier is given by [88–90]

$$\tilde{T} = \exp\left(-2 \int_{y_1}^{y_2} \kappa(y) dy \right), \tag{A8}$$

where y_1 and y_2 are the two classical turning points for the potential barrier, $\kappa(y) = \sqrt{2m[U_{\rm tot}(y) - E]}/\hbar$, and $U_{\rm tot}(y)$ is the form of the barrier in the total potential energy curve.

The average tunneling-limited lifetime of a trapped atom is then defined by

$$\tau_{\rm tun}(y_0) = \frac{1}{\Gamma_{\rm tun}(y_0)}. \tag{A9}$$

We calculated the tunneling loss rates for our model systems using the Gamow formalism described above. Figure 11 shows the resulting lifetimes $\tau_{\rm tun}$ calculated versus the position of the trap center y_0 from a graphene monolayer (red dashed curve) and a thin gold slab (yellow solid curve). The minimum distance that atoms can be trapped from the surface is marked by the left-hand ends of the two curves, where the tunnel barrier vanishes. Comparison of the curves shows that using a graphene monolayer reduces this distance to approximately 0.3 μm compared to the value of approximately 0.45 μm for the gold layer. For $y_0 > 0.5$ μm, the tunneling lifetime for the single layer of graphene is orders of magnitude higher than for the gold slab due to the weaker CP potential.

2. Atom losses due to Johnson noise

Magnetically trapped atoms only remain trapped when they are in a low-field seeking state with the magnetic moment aligned antiparallel to the direction of the magnetic field. In order to keep m_F a good quantum number, an offset magnetic field of a few gauss is typically maintained at the trapping position in atom-chip experiments [33]. Given a Zeeman splitting of, for example, 0.7 MHz/G for the ^{87}Rb ground state, this produces transition frequencies of a few megahertz between hyperfine states with different m_F values, thus making the trapped atoms susceptible to magnetic fields in that frequency range and therefore to noise in the radio-frequency domain.

Johnson noise arises from electrical noise currents within a conductor, which produce fluctuations of the magnetic field [91]. For near-surface traps formed between approximately 1 μm and 1 mm from a metallic conductor on a conventional atom chip, Johnson noise is usually the main limitation on the lifetime of the atom cloud [33,65,66]. For example, the measured lifetime of atoms trapped approximately 1 μm from thick metallic conductors is limited to only approximately 0.1 s by the effects of Johnson noise [33].

We now analyze and quantify the low Johnson noise produced by graphene, compared with metals, by using two models of increasing sophistication. First is a crude estimate based on previous models for metallic conductors and derived using the fluctuation-dissipation theorem [33,91,92]. Second, we present a rigorous quantum field theoretical calculation for 2D materials involving the full Green's function for the system, determined from the reflection coefficients for graphene and 2D multilayers.

Comparing graphene and gold wires with a given top surface area A, the ratio of the number of free electrons in graphene N_G to that in gold $N_{\rm Au}$ is $N_G/N_{\rm Au} = n_G/n_{\rm Au}t_{\rm Au}$, where $t_{\rm Au}$ is the thickness of the gold wire and n_G and $n_{\rm Au}$ are, respectively, the sheet and volume electron densities of undoped graphene and gold. Taking $n_{\rm Au} = 5.9 \times 10^{28}$ m^{-3} for bulk gold and typical values of $t_{\rm Au} = 1$ μm and $n_G = 9 \times 10^{14}$ m^{-2} [93] gives $N_G/N_{\rm Au} = 1.5 \times 10^{-8}$. The carrier mobility of gold is $\mu_{\rm Au} \approx 4.3 \times 10^{-3}$ m^2/V s and, in graphene, mobilities up to $\mu_G \approx 20$ m^2/V s have been reported in freestanding membranes [94,95]. For graphene on a substrate, the electron mobility is typically at least an order of magnitude lower, leading to the estimate $\mu_{\rm Au}/\mu_G \gtrsim 2 \times 10^{-4}$.

These results allow us to anticipate that the Johnson noise will be far smaller in graphene than in gold. Indeed, to make a rough initial estimate of this intuitive advantage, we now use the model presented in [33,91,92] to evaluate the expected spin-flip lifetime enhancement. For an atom trapped at distance d from a metal film of width $w \gg t$, where t is the thickness of the film, and resistivity ρ at temperature T, the $|F, m\rangle \to |F, m-1\rangle$ spin-flip rate, given in s^{-1}, is $\Gamma = C(T/\rho) \times [d(1 + d/t)(1 + 2d/w)]^{-1}$, where C is a constant that depends on the Clebsch-Gordon coefficient for the transition and on the transition frequency [33,91,92]. Assuming, as a crude initial approximation, that this formula can also be used to estimate the rate of spin flips induced by electrons in graphene, the ratio of the lifetimes τ_G and $\tau_{\rm Au}$ of atom clouds trapped at a distance d above graphene and gold wires, respectively, is

$$\frac{\tau_G}{\tau_{\rm Au}} = \frac{\Gamma_{\rm Au}}{\Gamma_G} = \frac{\rho_G}{\rho_{\rm Au}} \frac{1 + \frac{d}{t_G}}{1 + \frac{d}{t_{\rm Au}}}, \tag{A10}$$

where $t_G = 0.345$ nm is the thickness of a graphene monolayer, $\rho_{\rm Au} = 1/n_{\rm Au}e\mu_{\rm Au}$ and $\rho_G = t_G/n_G e\mu_G$ are the resistivities of the gold and graphene, respectively, and e is the electron charge.

Since $d \gg t_G$, it follows that

$$\frac{\tau_G}{\tau_{\rm Au}} \approx \left(\frac{n_{\rm Au}}{n_G}\right)\left(\frac{\mu_{\rm Au}}{\mu_G}\right)\frac{t_{\rm Au}d}{d + t_{\rm Au}} = \left(\frac{N_{\rm Au}}{N_G}\right)\left(\frac{\mu_{\rm Au}}{\mu_G}\right)\frac{d}{d + t_{\rm Au}}. \tag{A11}$$

Unless $d \ll t$, which is not the case for presently attainable trapping distances, the final term in the above equation is of order unity and so $\tau_G/\tau_{\rm Au}$ depends primarily on the relative number of free electrons in gold and in graphene and on their mobility ratio.

Using the values for the carrier mobility and density given above, we arrive at $\tau_G/\tau_{\rm Au} \gtrsim 1.3 \times 10^4 d/(d + t_{\rm Au})$. We thus predict that for atoms trapped approximately 1 μm away from a conductor, the lifetime will increase from approximately 0.1 s for a 1-μm-thick metallic wire, similar to that reported in [33], to greater than or approximately 600 s for graphene, i.e., an increase by a factor of $\tau_G/\tau_{\rm Au} \gtrsim 6.3 \times 10^3$. The physical reason for this is that although electrons in graphene have a higher mobility than in a metal, and so produce more Johnson noise per carrier, this is more than compensated by the far lower number of charge carriers in the graphene.

Below, we derive an expression for the Johnson noise produced by van der Waals heterostructures. To quantify the advantages of using 2D conductors, rather than metal wires, to reduce noise in atom chips we consider the particular case of graphene conduction channels. However, similar advantages are expected from other 2D materials due to their low number of electric current carriers.

The magnetic moment vector associated with the transition $|i\rangle \to |f\rangle$ of an atom is given by [96,97]

$$\boldsymbol{\mu} = -\langle i|\,\frac{\mu_B}{\hbar}\left(g_S\hat{\mathbf{S}} + g_L\hat{\mathbf{L}} - g_I\frac{m_{\rm e}}{m_{\rm nuc}}\hat{\mathbf{I}}\right)|f\rangle\,, \tag{A12}$$

where $\hat{\mathbf{S}}$, $\hat{\mathbf{L}}$, and $\hat{\mathbf{I}}$ are the electron spin operator, the electron orbital angular momentum operator, and the total nuclear angular momentum operator, respectively, with their corresponding Landé g factors g_S, g_L, and g_I; $m_{\rm e}$ is the electron mass; and $m_{\rm nuc}$ is the nuclear mass. Here the magnitude of the angular momentum, for example, $\hat{\mathbf{S}}$, is $\sqrt{S(S+1)}\hbar$ and the eigenvalue of the z component of $\hat{\mathbf{S}}$, i.e., $\hat{\mathbf{S}}_z$, is $m_S\hbar$, where S and m_S are the corresponding quantum numbers for $\hat{\mathbf{S}}$ and $\hat{\mathbf{S}}_z$, respectively.

Taking $L = 0$ for the electronic ground state and neglecting the term containing the total nuclear angular momentum operator $\hat{\mathbf{I}}$ in Eq. (A12) because $m_{\rm e} \ll m_{\rm nuc}$, the magnetic moment vector becomes $\boldsymbol{\mu} = -\mu_B g_S \langle i|\,\hat{\mathbf{S}}\,|f\rangle/\hbar$, where $g_S = 2$, and the rate of magnetic spin-flip transitions from an initial hyperfine magnetic state $|i\rangle$ to another state $|f\rangle$ is given by [97]

$$\Gamma_{\mathrm{JN}} = \mu_0 \frac{2(\mu_B g_S)^2}{\hbar^2} \sum_{j,k} \{ \langle f| \hat{\mathbf{S}}_j |i\rangle \langle i| \hat{\mathbf{S}}_k |f\rangle \times \mathrm{Im}[\nabla \times \nabla \times \mathbf{G}(\mathbf{r}_0, \mathbf{r}_0, \omega_{if})]_{jk} (\bar{n}_{\mathrm{th}} + 1)\}, \quad \text{(A13)}$$

where $\hat{\mathbf{S}}_{j,k}$ denotes the j and k components of the electron spin operator $\hat{\mathbf{S}}$ and $\mathbf{G}(\mathbf{r}_0, \mathbf{r}_0, \omega_{if})$ is the total dyadic Green's function describing the electromagnetic field of the transition frequency ω_{if} at $\mathbf{r}_0$ due to a *magnetic* dipole located at $\mathbf{r}_0$ (see Appendix B). The mean thermal photon occupation number is given by

$$\bar{n}_{\mathrm{th}} = \frac{1}{e^{\hbar\omega_{if}/k_B T} - 1}, \quad \text{(A14)}$$

where T is the temperature of the electromagnetic field system that causes the spin-flip transitions, rather than of the trapped atoms, and ω_{if} is the angular frequency of the radiation due to magnetic spin-flip transitions. The Johnson-noise lifetime of a single atom is defined as

$$\tau = \frac{1}{\Gamma_{\mathrm{JN}}}. \quad \text{(A15)}$$

Note that, mathematically, $\mathbf{G}(\mathbf{r}_0, \mathbf{r}_0, \omega_{if})$ can be written as the sum of a Green's tensor, describing the field due to a dipole in an infinitely extended homogeneous bulk medium, vacuum for example, and a scattering Green's tensor describing the reflected field in the presence of reflective bodies so that

$$\mathbf{G}(\mathbf{r}_0, \mathbf{r}_0, \omega_{if}) = \mathbf{G}^{(0)}(\mathbf{r}_0, \mathbf{r}_0, \omega_{if}) + \mathbf{G}^{(1)}(\mathbf{r}_0, \mathbf{r}_0, \omega_{if}). \quad \text{(A16)}$$

The explicit forms of $\mathbf{G}^{(0)}(\mathbf{r}_0, \mathbf{r}_0, \omega_{if})$ can be found in [98,99] and are summarized in Appendix B. Owing to the general properties of a Green's tensor, we have

$$\mathrm{Im}[\nabla \times \nabla \times \mathbf{G}(\mathbf{r}, \mathbf{r}_0, \omega)] = \frac{\omega^2}{c^2} \mathrm{Im}[\epsilon(\omega)\mu(\omega)\mathbf{G}(\mathbf{r}, \mathbf{r}_0, \omega)], \quad \text{(A17)}$$

where $\epsilon(\omega)$ and $\mu(\omega)$ are, respectively, the permittivity and permeability of the medium in which the field and source points are located. The imaginary part of the Green's tensor in vacuum has a simple form

$$\mathrm{Im}[\mathbf{G}^{(0)}(\mathbf{r}_0, \mathbf{r}_0, \omega)]_{jk} = \frac{1}{6\pi} \frac{\omega}{c} \delta_{jk}, \quad \text{(A18)}$$

where δ_{jk} is the Kronecker delta, which allows us to determine the spin-flip rates in vacuum.

In this Appendix we use Eq. (1) to determine an appropriate value of the atomic transition frequency for input into our Johnson-noise lifetime calculations in the presence of the magnetic trapping field. For the $|F, m_F\rangle = |2, 2\rangle$, $5\,^2S_{1/2}$ ground state of the ^{87}Rb atoms considered here, $g_F = \frac{1}{2}$ [79,96]. Here we only consider the Zeeman transition from $|2, 2\rangle$ to $|2, 1\rangle$ to facilitate direct comparison with the results of Ref. [33]. The angular frequency of the radiation is then given by

$$\omega_{if} = \frac{\mu_B |\mathbf{B}(\mathbf{r}_0)|}{2\hbar}. \quad \text{(A19)}$$

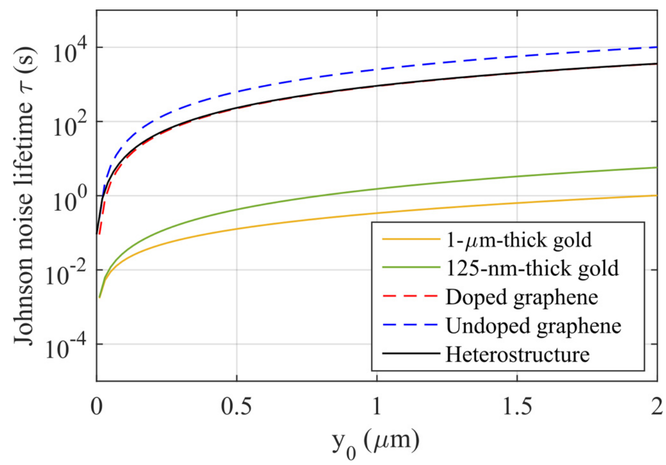

FIG. 12. Johnson-noise lifetimes τ calculated [using Eqs. (A13) and (A15)] versus the position of the harmonic trap center y_0 for an ultracold gas of ^{87}Rb atoms trapped above: an undoped graphene monolayer (blue dashed curve), a doped graphene monolayer with Fermi energy $E_F = 0.1$ eV (red dashed curve), an hBN-encased graphene-based heterostructure (black solid curve), a 1-μm-thick gold slab (yellow solid curve), and a 125-nm-thick gold slab (green solid curve). The graphene monolayers yield orders of magnitude longer lifetimes than the 1-μm-thick gold slab because they have far lower electromagnetic reflectance than gold (see the text). The parameters are $T = 300$ K and $\omega = 2\pi \times 560$ kHz.

Taking $|\mathbf{B}(\mathbf{r}_0)| = 0.8 \times 10^{-4}$ T gives $\omega_{if} = 2\pi \times 560$ kHz. Comparing with the hyperfine splitting frequency for the ground state of the ^{87}Rb atom, which is $2\pi \times 6.83$ GHz, we now see that our assumption that m_F is a good quantum number is justified. The method for calculating the Clebsch-Gordon coefficients associated with the spin-flip transition matrix elements $\langle f| \hat{\mathbf{S}}_{j,k} |i\rangle$ can be found in [100]. For completeness, we note that these matrix elements are

$$\begin{aligned} \langle 2,2| \hat{\mathbf{S}}_x |2,1\rangle &= \langle 2,1| \hat{\mathbf{S}}_x |2,2\rangle = \frac{1}{4}, \\ \langle 2,2| \hat{\mathbf{S}}_y |2,1\rangle &= -\langle 2,1| \hat{\mathbf{S}}_y |2,2\rangle = \frac{i}{4}, \\ \langle 2,2| \hat{\mathbf{S}}_z |2,1\rangle &= \langle 2,1| \hat{\mathbf{S}}_z |2,2\rangle = 0. \end{aligned} \quad \text{(A20)}$$

To proceed with our calculations of the transition rates and comparisons for different surface materials, we consider the typical thickness of the metallic wires used to generate the magnetic field in atom chips, which is approximately 1 μm [33]. Figure 12 shows the Johnson-noise-limited lifetimes of the atom cloud τ calculated versus atom-surface distance y_0 for a 1-μm-thick gold slab (yellow solid curve), a 125-nm-thick gold slab (green solid curve), a doped graphene monolayer with $E_F = 0.1$ eV (red dashed curve), an undoped graphene monolayer (blue dashed curve), and a heterostructure consisting of a graphene monolayer encased by two 10-nm-thick hBN layers (black solid curve). Note that to facilitate comparison with the lifetimes reported in [33], Fig. 12 is calculated using Eqs. (A13) and (A15). The graphene monolayers yield far longer lifetimes than the gold wires do, even for a small wire thickness of 125 nm. Making gold wires thinner than 125 nm is possible, but their resistivities then become higher than for bulk gold [86]. Silver wires a few tens of nanometers thick have been made [101], but exhibit graininess on length scales comparable to the film thickness, varying from approximately 8 nm for 20-nm-thick films to approximately 40 nm when the film size reaches 60 nm. Moreover, wires made from silver would be prone to oxidization, which would affect their conductivity. At $y_0 = 1\ \mu$m, the lifetimes for the undoped graphene monolayer and the 1-μm-thick gold slab are approximately 2500 and 0.34 s, respectively, giving a lifetime ratio of approximately 7.4×10^3, which is broadly consistent with the estimate of approximately 6.3×10^3 obtained from Eq. (A10). The lifetime for the heterostructure is slightly longer than that for the doped graphene layer.

We conclude that Johnson noise in graphene conductors will produce negligible spin-flip losses compared to the thick ($t_{\mathrm{Au}} \sim 1\ \mu$m) metal wires typically used in atom chips, where it dominates the loss rate. Consequently, our analysis of graphene atom chips will henceforth focus on the effects of tunneling and three-body losses and of spatial imperfections. We note, however, from Eq. (A10) that the lifetime above metallic conductors can be increased by decreasing their thickness t_{Au} and hence N_{Au}. For wires with $t_{\mathrm{Au}} =$ 125 nm, $\tau_G/\tau_{\mathrm{Au}} \sim 1400$. Taking the limit of the gold layer thickness to its lattice constant, 0.4 nm, gives $\tau_G/\tau_{\mathrm{Au}} \sim 5$. So the advantage of graphene over metallic conductors persists even if the metal wire could be thinned close to the theoretical limit of a monolayer. However, graphene and other exfoliated van der Waals materials are the only monolayers so far produced. Moreover, their hexagonal crystal structure and resulting lightlike linear energy band dispersion relations ensure that they can carry high currents despite their low thickness and carrier density. However, if high-quality metallic monolayers could be produced, their low electron density may reduce the Johnson noise and Casimir-Polder potential to levels comparable to exfoliated 2D materials.

3. Negligible corrugation effects

Spatial meandering of the current stream lines can in principle be created in four ways: deviation from strictly two-dimensional current flow (analogous to surface roughness of 3D conductors), edge roughness resulting from imperfect lithography, electrons scattering from one another or from phonons, and spatial variations in the electron potential energy created by impurities or imperfections in or near the conducting channel [41,42,102–104]. We now consider the importance of each potential source of roughness in turn.

When graphene is encapsulated in hBN, the surface roughness and non-two-dimensionality in graphene is only of order 12 pm [105] because the hBN provides an ultraflat surface for the graphene and is closely lattice matched to it [106–108]. Such low roughness is consistent with that of an individual graphene layer in bulk graphite and will have a negligible effect on the atom-trapping potential landscape. Edge roughness will be determined by the quality of the lithography used to define and create the conducting channels. Since graphene is two dimensional, there will be negligible vertical fluctuations in the channel wall. Edge fluctuations along the channel will be determined by the lithographic process used and comparable to those in existing atom chips with metallic conductors. For electron beam lithography, the edge fluctuations will be of order 35 nm [109], whereas for helium ion beams, values below 5 nm are attainable [110].

In metallic conductors, grain boundaries give rise to local electron scattering processes, which can be detected via their effect on the current flow pattern and resulting modulation of the trapping potential and BEC atom density [41,42,110,111]. By contrast, graphene monolayers contain no grains to induce position-specific scattering processes and resulting atom density fluctuations. Electron-electron and electron-phonon scattering events do occur, but these are spatiotemporally stochastic, rather than occurring at particular fixed positions within the conducting channel, and therefore will not produce roughness in the trapping potential and BEC density profile because of time averaging. Moreover, since their characteristic length scales are shorter than the typical dimensions of atom-chip wires, ballistic transport effects do not need to be considered. However, electron scattering mechanisms do affect the diffusive electron mobility and hence the Johnson-noise-limited spin-flip lifetime of the trapped atom cloud.

Spatial fluctuations in the electronic potential energy created by imperfections and impurities that either are within the graphene or accumulate at interfaces in hBN-encased graphene structures have been studied theoretically and measured in resonant-tunneling experiments [107,112–116]. Self-consistent calculations [114,115], which give excellent quantitative agreement with measurements of graphene's electron mobility μ_G versus impurity density and with scanning probe surface studies [113], predict that the correlation length of these potential fluctuations is approximately 10 nm. Recent experiments on graphene and boron nitride tunnel transistors have shown that for graphene monolayers encased by several layers of hBN, the correlation length is approximately 12 nm [112,117]. Consequently, the associated small-angle current meander will have negligible effect on the potential landscape of atoms trapped even as close as 150 nm from the graphene and will therefore not influence the minimum atom-surface trapping distance.

When graphene is placed or grown epitaxially on hBN, the small lattice mismatch between the two materials gives rise to a strain-induced moiré pattern and superlattice potential, which can modify the electronic properties of electrons within the graphene. Moiré periods up to 80 nm have been realized [118] and further increases in period may modulate the current flow on a length scale long enough to produce detectable variation in the density profile of a BEC trapped nearby. Such variations could yield information about the superlattice potential and the underlying strain mechanisms.

APPENDIX B: DYADIC GREEN'S FUNCTION

In this Appendix we discuss the Green's tensors for planar multilayer systems, like those considered in the main text. We will start by considering the general characteristics of an electric field in a homogeneous space, in order to provide an intuitive explanation of the Green's tensors.

1. General definition

Let us recall the inhomogeneous Helmholtz equation describing the relationship between an electric field **E** and a current density $\mathbf{j}$ of angular frequency ω at position $\mathbf{r}$ with respect to a linear, isotropic, inhomogeneous medium, with relative magnetic permeability $\mu(\omega)$ and relative permittivity $\epsilon(\omega)$ [119,120]:

$$\nabla \times \nabla \times \mathbf{E}(\omega, \mathbf{r}) - k^2\mathbf{E}(\omega, \mathbf{r}) = i\omega\mu_0\mu\mathbf{j}(\omega, \mathbf{r}). \tag{B1}$$

Here $k = \sqrt{\epsilon(\omega)\mu(\omega)\omega^2/c^2}$ is the magnitude of the wave vector associated with the electromagnetic wave, μ_0 is the permeability of free space, and

$$\mathbf{j}(\omega, \mathbf{r}) = j_x(\omega, \mathbf{r})\mathbf{e}_x + j_y(\omega, \mathbf{r})\mathbf{e}_y + j_z(\omega, \mathbf{r})\mathbf{e}_z, \tag{B2}$$

where $\mathbf{e}_x$, $\mathbf{e}_y$, and $\mathbf{e}_z$ are the unit vectors in the x, y, and z directions, respectively, with j_x, j_y, and j_z the corresponding current density components.

The classical Green's tensor $\mathbf{G} = (\mathbf{G}_x, \mathbf{G}_y, \mathbf{G}_z)$, as a function of the field point position $\mathbf{r}$, the source point position $\mathbf{r}'$, and the wave angular frequency ω, is the unique solution to the differential equations

$$\nabla \times \nabla \times \mathbf{G}_x(\mathbf{r}, \mathbf{r}', \omega) - k^2\mathbf{G}_x(\mathbf{r}, \mathbf{r}', \omega) = \delta(\mathbf{r} - \mathbf{r}')\mathbf{e}_x, \tag{B3}$$

$$\nabla \times \nabla \times \mathbf{G}_y(\mathbf{r}, \mathbf{r}', \omega) - k^2\mathbf{G}_y(\mathbf{r}, \mathbf{r}', \omega) = \delta(\mathbf{r} - \mathbf{r}')\mathbf{e}_y, \tag{B4}$$

$$\nabla \times \nabla \times \mathbf{G}_z(\mathbf{r}, \mathbf{r}', \omega) - k^2\mathbf{G}_z(\mathbf{r}, \mathbf{r}', \omega) = \delta(\mathbf{r} - \mathbf{r}')\mathbf{e}_z, \tag{B5}$$

where $\delta(\mathbf{r} - \mathbf{r}')$ is the Dirac delta function. These three Green's functions, in a column vector form, can be combined into a single tensor, giving the general definition of the dyadic Green's function (Green's tensor) for the electric field

$$\nabla \times \nabla \times \mathbf{G}(\mathbf{r}, \mathbf{r}', \omega) - k^2\mathbf{G}(\mathbf{r}, \mathbf{r}', \omega) = \mathbf{I}\delta(\mathbf{r} - \mathbf{r}'), \tag{B6}$$

where $\mathbf{I}$ is the unit dyad (unit tensor).

We can see that each column of the tensor $\mathbf{G}$ can be mathematically treated individually: The curl operators can be applied to any column of the Green's tensor as if they were to act on a single column vector. In addition, each column can be interpreted separately: The first column of the Green's tensor describes the field due to a point source in the x direction, the second column the field due to a point source in the y direction, and the third column the field due to a point source in the z direction. Consequently, a particular solution of Eq. (B1) defined by the dyadic Green's function is

$$\mathbf{E}(\omega, \mathbf{r}) = i\omega\mu\mu_0 \int_V \mathbf{G}(\mathbf{r}, \mathbf{r}', \omega)\mathbf{j}(\omega, \mathbf{r}')d^3r', \tag{B7}$$

where the integral is evaluated over the volume V of the current source body (see Fig. 13).

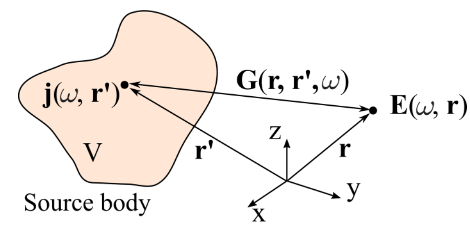

FIG. 13. Illustration of the dyadic Green's function $\mathbf{G}(\mathbf{r}, \mathbf{r}', \omega)$. The Green's function relates the local current source $\mathbf{j}$ at point $\mathbf{r}'$ and the associated electric field $\mathbf{E}$ at point $\mathbf{r}$. The total electric field is the superposition of every field corresponding to each point source in the source body of volume V.

2. Green's tensor for planar multilayer systems

Let us consider the situation shown in Fig. 7, where a radiating electric dipole is located above a layered substrate. We assume that the upper half space is vacuum, while the lower half space (atom-chip substrate) is optically denser.

Since the electric field in layer 1 is the superposition of the field directly radiated from the dipole and the field scattered by the material layers, the Green's function can, correspondingly, be decomposed into two contributions: a Green's function for homogeneous space and a scattering Green's function reflecting dielectric inhomogeneity. In order to find the primary dyadic Green's function $\mathbf{G}^{(0)}(\mathbf{r}, \mathbf{r}', \omega)$ (sometimes called the free-space Green's function), we remove the interfaces in Fig. 7 and assume that the electric dipole $\mathbf{d}$, located at $\mathbf{r}' = (x', y', z')$, is in a homogeneous, linear, and isotropic medium, characterized by permittivity and permeability functions $\epsilon_1(\omega)$ and $\mu_1(\omega)$. The superscript (0) here is to remind us that this Green's function is the primary Green's function. The associated electric field at $\mathbf{r} = (x, y, z)$ and its corresponding wave vectors are

$$\mathbf{E}(\mathbf{r}, \omega) = \omega^2\mu_0\mu_1\mathbf{G}^{(0)}(\mathbf{r}, \mathbf{r}', \omega)\mathbf{d}(\mathbf{r}', \omega), \tag{B8}$$

$$\mathbf{k}_1(\omega) = k_x\mathbf{e}_x + k_{y1}\mathbf{e}_y + k_z\mathbf{e}_z = k^{\parallel}\mathbf{e}_{k^{\parallel}} + k_{y1}\mathbf{e}_y, \tag{B9}$$

respectively, where k_x and k_z are the x and z components of the wave vector $k^{\parallel}\mathbf{e}_{k^{\parallel}} = k_x\mathbf{e}_x + k_z\mathbf{e}_z$ in the x-z plane, which are the same in every layer, and k_{y1} is the y component of the wave vector in layer 1.

The primary Green's tensor can be written in the form [74,98,99]

$$\mathbf{G}^{(0)}(\mathbf{r}, \mathbf{r}', \omega) = \frac{i}{8\pi^2} \iint_{-\infty}^{\infty} \frac{1}{k_{y1}}\mathbf{M}^{(0)}(k_x, k_z) \times e^{i[k_x(x-x')+k_z(z-z')+k_{y1}|y-y'|]}dk_x dk_z, \tag{B10}$$

in which

$$\mathbf{M}^{(0)}(k_x, k_z) = (\mathbf{e}_{s\pm} \otimes \mathbf{e}_{s\pm}) + (\mathbf{e}_{p\pm} \otimes \mathbf{e}_{p\pm}), \tag{B11}$$

where $\otimes$ represents a tensor product. Here the polarization unit vectors for s- and p-polarized waves in layer 1 are defined as (see Fig. 14)

$$\mathbf{e}_{s\pm} = \mathbf{e}_{k^{\parallel}} \times \mathbf{e}_y, \tag{B12}$$

$$\mathbf{e}_{p\pm} = \frac{1}{k_1}(k^{\parallel}\mathbf{e}_y \mp k_{y1}\mathbf{e}_{k^{\parallel}}), \tag{B13}$$

where $k_1 = \sqrt{\epsilon_1(\omega)\mu_1}(\omega)\omega/c = (k_{y1}^2 + k^{\parallel 2})^{1/2}$ is the wave number and the upper ($-$) sign applies for $y > y'$ (i.e., waves propagating in the positive y direction), while the lower ($+$) sign applies for $y < y'$ (i.e., waves propagating in the negative y direction).

Let us now consider what happens to the electric field described by the above primary Green's function when a reflective planar layered structure is added to the system below the dipole, as depicted in Fig. 7. Physically, the role of the layered structure is to reflect back the electromagnetic wave radiated from the dipole. Therefore, mathematically, multiplying the individual incident plane waves in $\mathbf{G}^{(0)}$ with the

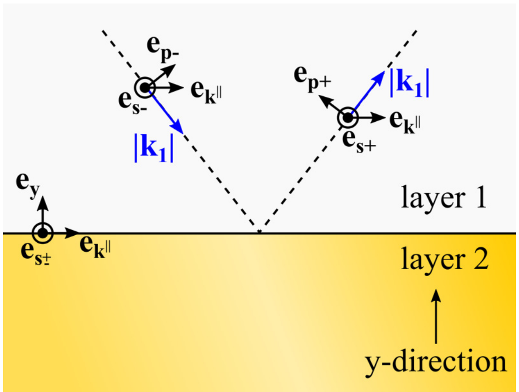

FIG. 14. Definition of the polarization unit vectors. The plane spanned by the vector $\mathbf{e}_y$, pointing in the positive y direction, and the vector $\mathbf{e}_{k^\parallel} = (k_x, 0, k_z)/k^\parallel$ defines the plane of incidence. The s-polarization unit vectors $\mathbf{e}_{s\pm}$ are perpendicular to the plane of incidence, while the p-polarization unit vectors $\mathbf{e}_{p\pm}$ are parallel to the plane of incidence and perpendicular to the directions of propagation (blue arrows).

corresponding generalized Fresnel reflection coefficients $r_s^{(1)}$ and $r_p^{(1)}$, along with changing the phase factor (the exponential term) accordingly, yields the scattering Green's tensor

$$\mathbf{G}^{(1)}(\mathbf{r},\mathbf{r}',\omega) = \frac{\mathrm{i}}{8\pi^2}\iint_{-\infty}^{\infty}\frac{1}{k_{y1}}\mathbf{M}^{(1)}(k_x,k_z) \times e^{i[k_x(x-x')+k_z(z-z')+k_{y1}(y+y')]}dk_x dk_z, \quad \text{(B14)}$$

where

$$\mathbf{M}^{(1)}(k_x,k_z) = r_s^{(1)}(\mathbf{e}_{s+}\otimes\mathbf{e}_{s-}) + r_p^{(1)}(\mathbf{e}_{p+}\otimes\mathbf{e}_{p-}). \quad \text{(B15)}$$

Here the superscript (1) is to remind us that the Green's tensor is the scattering Green's tensor for layer 1.

The total electric field due to a radiating *electric* dipole above a planar structure can now be written as

$$\mathbf{E}(\mathbf{r},\omega) = \omega^2\mu_0\mu_1\mathbf{G}_E(\mathbf{r},\mathbf{r}',\omega)\mathbf{d}(\mathbf{r}',\omega), \quad \text{(B16)}$$

where $\mathbf{G}_E(\mathbf{r},\mathbf{r}',\omega) = \mathbf{G}^{(0)}(\mathbf{r},\mathbf{r}',\omega) + \mathbf{G}^{(1)}(\mathbf{r},\mathbf{r}',\omega)$ and we introduce a subscript E to emphasize that this Green's function is for an electric dipole. In order to obtain a scattering Green's tensor for a *magnetic* dipole, we interchange the Fresnel reflection coefficients in (B11).

The relevant Green's tensors for calculating the CP potential and the Johnson noise must be evaluated at $\mathbf{r} = \mathbf{r}' = \mathbf{r}_0$, where $\mathbf{r}_0 = (x_0, y_0, z_0)$ is the position of the center of the magnetic trap. After straightforward manipulation of the polar coordinates, the equal-position scattering Green's tensor is therefore given by [75,99]

$$\mathbf{G}^{(1)}(\mathbf{r}_0,\mathbf{r}_0,\omega) = \frac{i}{8\pi}\int_0^\infty dk^\parallel\frac{k^\parallel}{k_{y1}}e^{2ik_{y1}y_0} \times\left[\mathbf{M}_\alpha r_s^{(1)}(k^\parallel,\omega) + \frac{c^2}{\omega^2}\mathbf{M}_\beta r_p^{(1)}(k^\parallel,\omega)\right], \quad \text{(B17)}$$

where y_0 is the shortest distance between the surface and the center of the magnetic trap and

$$k_{y1} = \left(\mu_1\epsilon_1\frac{\omega^2}{c^2} - k^{\parallel 2}\right)^{1/2}, \quad \text{(B18)}$$

with $k^{\parallel 2} = k_x^2 + k_z^2$. The tensors $\mathbf{M}_\alpha$ and $\mathbf{M}_\beta$ in Eq. (B17) are given by

$$\mathbf{M}_\alpha = \begin{pmatrix} 1 & 0 & 0 \\ 0 & 0 & 0 \\ 0 & 0 & 1 \end{pmatrix}, \quad \text{(B19)}$$

$$\mathbf{M}_\beta = \begin{pmatrix} -k_{y1}^2 & 0 & 0 \\ 0 & 2k^{\parallel 2} & 0 \\ 0 & 0 & -k_{y1}^2 \end{pmatrix}. \quad \text{(B20)}$$

Note that the forms of $\mathbf{M}_\alpha$ and $\mathbf{M}_\beta$ depend on the coordinate system used and that Eq. (B17) only describes an electromagnetic field with a *real* frequency, created by a radiating electric dipole.

For a purely imaginary frequency $\omega = i\xi$, where ξ is real, e.g., the Matsubara frequencies that appear in the CP potential calculations, the wave vector in the direction perpendicular to the surface is always purely imaginary, $k_{y1} = \mathrm{i}\kappa_1^\perp$, with

$$\kappa_1^\perp(\mu_1,\epsilon_1,i\xi) = \sqrt{\mu_1(i\xi)\epsilon_1(i\xi)\frac{\xi^2}{c^2} + k^{\parallel 2}} \quad \text{(B21)}$$

and

$$k^\parallel = \sqrt{\kappa_1^{\perp 2} - \mu_1\epsilon_1\frac{\xi^2}{c^2}} = \sqrt{\kappa_l^{\perp 2} - \mu_l\epsilon_l\frac{\xi^2}{c^2}}, \quad \text{(B22)}$$

where the subscript l denotes the layer index corresponding to each wave vector. Equations (B21) and (B22) tell us that the wave numbers in the direction perpendicular to the surface are functions of the optical properties of the materials and the incident wave frequencies, whereas the wave numbers in the direction parallel to the surface are constant for a given $\kappa_l^\perp$. The equal-position Green's tensor for *purely imaginary* frequencies is then given by [98,99,120]

$$\mathbf{G}^{(1)}(\mathbf{r}_0,\mathbf{r}_0,i\xi) = \frac{1}{8\pi}\int_{\xi/c}^\infty d\kappa_1^\perp e^{-2\kappa_1^\perp y_0} \times\left[\mathbf{M}_\alpha r_s^{(1)}(k^\parallel,i\xi) - \frac{c^2}{\xi^2}\mathbf{M}_\beta r_p^{(1)}(k^\parallel,i\xi)\right]. \quad \text{(B23)}$$

Finally, we note that the Green's tensor for a magnetic dipole, which is needed for the Johnson-noise calculations, can be readily obtained by interchanging the reflection coefficients in (B17).

APPENDIX C: OPTICAL PROPERTIES OF MATERIALS

In this Appendix we briefly introduce the optical properties of graphene, hBN, and bulk gold. They are used in order to determine the behavior of the reflection coefficients of our system (see Appendix D).

Graphene's optical conductivity can be split into two distinct contributions. The first describes how the charge carriers respond to electromagnetic radiation by transitioning to higher-energy states within the same energy bands without conserving momentum [intraband transitions $\sigma_{\text{intra}}(\omega)$]. The second accounts for vertical momentum-conserving transitions from the valence band to the conduction band, induced by the electromagnetic radiation [interband transitions $\sigma_{\text{inter}}(\omega)$], where ω is the angular frequency of the electromagnetic field to which the graphene is exposed.

The expression for graphene's conductivity has been considered using multiple approaches and limits (see, for example, [121,122]) and the choice of a specific description depends on the features of the system under analysis and/or on the particular aspect under investigation (see, for example, [123–126] and the references below). For our systems and its parameters we can use the expression derived from the Kubo formula [74,127,128], which gives

$$\sigma_{\text{intra}}(\omega) = \frac{\sigma_0}{\pi}\frac{4}{\hbar\gamma - i\hbar\omega}[E_F + 2k_BT\ln(1+e^{-E_F/k_BT})], \tag{C1}$$

$$\sigma_{\text{inter}}(\omega) = \sigma_0\left[G\left(\frac{\hbar\omega}{2}\right) + i\frac{4\hbar\omega}{\pi}\int_0^\infty dE\,\frac{G(E)-G(\frac{\hbar\omega}{2})}{(\hbar\omega)^2-4E^2}\right], \tag{C2}$$

in which

$$G(X) = \frac{\sinh\left(\frac{X}{k_BT}\right)}{\cosh\left(\frac{E_F}{k_BT}\right)+\cosh\left(\frac{X}{k_BT}\right)}, \tag{C3}$$

where $\sigma_0 = e^2/4\hbar$ is the universal alternating-current conductivity of graphene, γ is the electron relaxation rate in graphene, E_F is the Fermi energy, and T is the temperature of the graphene layer.

Within the four-parameter semiquantum model [129–132], the in-plane optical conductivity of an ultrathin hBN slab comprising a few monolayers is

$$\sigma_{\text{hBN}}(i\xi_j) = i\epsilon_0\xi_j t_{\text{hBN}}[\epsilon_{z,\text{hBN}}(i\xi_j) - \epsilon_z(\infty)]. \tag{C4}$$

Here the frequency-dependent permittivity of hBN is given by

$$\epsilon_{f,\text{hBN}}(i\xi_j) = \epsilon_f(\infty) + \frac{s_{v,f}\,\omega_{v,f}^2}{\omega_{v,f}^2 + \gamma_{v,f}\xi_j + \xi_j^2}, \tag{C5}$$

where $f = x, y, z$; $\omega_{v,z} = 2.58\times10^{14}$ rad/s; $\gamma_{v,z} = 1.319\times10^{12}$ rad/s; $s_{v,z} = 1.83$; $\epsilon_z(\infty) = 4.87$ (see the supplementary information of [133]); and t_{hBN} is the thickness of the hBN slab. For metals, in particular gold, we use the Drude model for the permittivity

$$\epsilon_{\text{metal}}(i\xi_j) = 1 + \frac{\omega_{\text{p}}^2}{\xi_j^2 + \Gamma_D\xi_j}, \tag{C6}$$

where, for gold, $\omega_{\text{p}} = 1.38\times10^{16}$ rad/s is the plasma frequency and $\Gamma_D = 1.075\times10^{14}$ rad/s is the electron relaxation rate [98,134].

APPENDIX D: REFLECTION COEFFICIENTS

Typical atom chips can be modeled as planar multilayer structures (see Fig. 7) with generalized Fresnel reflection coefficients given by the recursive relations [99,135]

$$\begin{aligned} r_s^{(l)} &= r_s^{(l)}(k^\parallel, \omega = i\xi_j) \\ &= \frac{a + \{b\exp(2ik_{yl+1}^\perp t_{l+1})r_s^{(l+1)}\}}{b + \{a\exp(2ik_{yl+1}^\perp t_{l+1})r_s^{(l+1)}\}}, \end{aligned} \tag{D1}$$

$$\begin{aligned} r_p^{(l)} &= r_p^{(l)}(k^\parallel, \omega = i\xi_j) \\ &= \frac{c + \{d\exp(2ik_{yl+1}^\perp t_{l+1})r_p^{(l+1)}\}}{d + \{c\exp(2ik_{yl+1}^\perp t_{l+1})r_p^{(l+1)}\}}, \end{aligned} \tag{D2}$$

where $a = (\mu_{l+1}k_{yl} - \mu_l k_{yl+1})$, $b = (\mu_{l+1}k_{yl} + \mu_l k_{yl+1})$, $c = (\epsilon_{l+1}k_{yl} - \epsilon_l k_{yl+1})$, and $d = (\epsilon_{l+1}k_{yl} + \epsilon_l k_{yl+1})$ for $l = 1, \ldots, n-1$ with $\mu_l = \mu_l(i\xi)$, $\epsilon_l = \epsilon_l(i\xi)$, and a termination condition $r_{s,p}^n = 0$. Here k_{yl} is defined in the same manner as Eqs. (B21) and (B22). Note that the superscripts (l) on r_s and r_p are indices denoting which layers the reflection coefficients correspond to. We use this method to calculate the reflection coefficients of the metallic conducting wires.

Another way to determine the reflection coefficients is to use a transfer-matrix method (see, for example, [71]). We use this as a convenient method to calculate the reflection coefficients of the structures that incorporate graphene layers. We now present a concise description of this method. There are two basic elements in this formalism, namely, transmission matrices and propagation matrices: A transmission matrix describes the change of the wave amplitudes when the wave crosses an interface between two media, whereas a propagation matrix captures the phase change when the wave propagates through a medium. Important physical quantities in this method are the conductivities of the ultrathin layers and the permittivities of thick media.

Let us consider the scattering of electromagnetic waves of frequency ω, scatter from a planar structure consisting of a monolayer graphene, cladded by two semi-infinite dielectric media of relative permittivities ϵ_1 and ϵ_2, as shown in Fig. 15. The graphene sheet is located in the $y = 0$ plane and is assumed to be infinitesimally thin such that medium 1 (characterized by a relative permittivity ϵ_1) occupies the region defined by $y > 0$ and medium 2 (characterized by a relative permittivity ϵ_2) occupies the region defined by $y < 0$. Let us further assume that the waves are plane waves, that their **B** field only has an x component, and that their **E** field is parallel to the plane of incidence, which coincides with the y-z plane (commonly known as transverse magnetic waves or p-polarized waves). Therefore, the **B** fields can be written as

$$\mathbf{B}_x^{(j)}(\mathbf{r},\mathbf{t}) = (A_j e^{-ik_{j,y}y} + B_j e^{ik_{j,y}y})e^{i(k_{j,z}z-\omega t)}\hat{\mathbf{x}}, \tag{D3}$$

where $j = 1, 2$ are for the waves in medium 1 and medium 2, respectively; A_j and B_j are the amplitudes of the waves propagating in the negative and positive y directions, respectively; subscripts x, y, and z denote the components associated with the coordinate axes; t is time; $\hat{\mathbf{x}}$ is a unit vector pointing in the positive x direction (out of the page); and the relation between

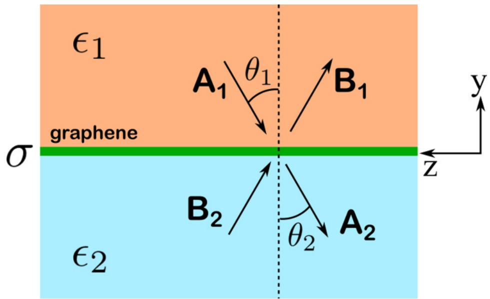

FIG. 15. Schematic diagram of electromagnetic scattering in a structure composed of a single graphene sheet (green) sandwiched by two semi-infinite dielectric media of relative permittivities ϵ_1 (orange) and ϵ_2 (blue). The graphene sheet is located at the plane defined by $y = 0$ and its electromagnetic properties are encompassed by a conductivity σ. Arrows, all lying in a plane called the plane of incidence, which coincides with the y-z plane, indicate the propagation directions of the electromagnetic waves (denoted by A_1 and A_2 for traveling towards the negative y direction and by B_1 and B_2 for the positive y direction). Here θ_1 and θ_2 are the incident and refracted angles, respectively.

the y and z components of the wave vector is given by

$$k_{j,y}^2 = \epsilon_j \frac{\omega^2}{c^2} - k_{j,z}^2. \tag{D4}$$

In dielectric media, the relation between **B** and **E** fields is given by the Maxwell equation

$$\nabla \times \mathbf{B} = -i\frac{\epsilon\omega}{c^2}\mathbf{E}. \tag{D5}$$

Using the equation given above, the z component of the **E** fields is found to be

$$\mathbf{E}_z^{(j)}(\mathbf{r}, \mathbf{t}) = \frac{-k_{j,y}c^2}{\omega\epsilon_j}(A_j e^{-ik_{j,y}y} - B_j e^{ik_{j,y}y})e^{i(k_{j,z}z-\omega t)}\hat{\mathbf{z}}, \tag{D6}$$

where $\hat{\mathbf{z}}$ is a unit vector pointing in the positive z direction.

In order to find the relations between the amplitudes of the waves in medium 1 and medium 2, we need to invoke the boundary conditions at the interface between the two dielectric media for the parallel components of **E** and **B** fields, which are

$$\hat{\mathbf{n}} \times (\mathbf{E}^{(1)} - \mathbf{E}^{(2)}) = 0, \tag{D7}$$

$$\hat{\mathbf{n}} \times (\mathbf{B}^{(1)} - \mathbf{B}^{(2)}) = \mu_0 \mathbf{J}_s, \tag{D8}$$

where $\hat{\mathbf{n}}$ is a normal unit vector pointing from medium 2 into medium 1 (equivalent to $\hat{\mathbf{y}}$) and $\mathbf{J}_s$ is the free surface current density at the boundary, which is the graphene sheet in this case. Writing out only the relevant components and using the generalized Ohm law $\mathbf{J} = \sigma\mathbf{E}$, we obtain

$$E_z^{(1)}(y = 0) = E_z^{(2)}(y = 0), \tag{D9}$$

$$B_x^{(1)}(y = 0) - B_x^{(2)}(y = 0) = \mu_0\sigma E_z^{(1)}(y = 0), \tag{D10}$$

where σ is the optical conductivity of the 2D material at the interface (graphene). Substituting Eqs. (D3) and (D6) into the above boundary conditions yields

$$A_1 - B_1 = \frac{\epsilon_1 k_{2,y}}{\epsilon_2 k_{1,y}}(A_2 - B_2), \tag{D11}$$

$$A_1 + B_1 = (A_2 + B_2) + \frac{\sigma k_{2,y}}{\omega\epsilon_0\epsilon_2}(A_2 - B_2). \tag{D12}$$

Converting (D11) and (D12) into a matrix equation yields

$$\begin{pmatrix} 1 & -1 \\ 1 & 1 \end{pmatrix}\begin{pmatrix} A_1 \\ B_1 \end{pmatrix} = \begin{pmatrix} \eta_p & -\eta_p \\ 1+\xi_p & 1-\xi_p \end{pmatrix}\begin{pmatrix} A_2 \\ B_2 \end{pmatrix}, \tag{D13}$$

where the following functions have been introduced to simplify our notation:

$$\eta_p = \frac{\epsilon_1 k_{2,y}}{\epsilon_2 k_{1,y}}, \quad \xi_p = \frac{\sigma k_{2,y}}{\omega\epsilon_0\epsilon_2}. \tag{D14}$$

Multiplying (D13) by the inverse of the leftmost matrix of (D13), we obtain a transfer-matrix equation

$$\begin{pmatrix} A_1 \\ B_1 \end{pmatrix} = \frac{1}{2}\begin{pmatrix} 1+\eta_p+\xi_p & 1-\eta_p-\xi_p \\ 1-\eta_p+\xi_p & 1+\eta_p-\xi_p \end{pmatrix}\begin{pmatrix} A_2 \\ B_2 \end{pmatrix} \tag{D15}$$

$$= \mathbf{T}_p\begin{pmatrix} A_2 \\ B_2 \end{pmatrix}, \tag{D16}$$

where

$$\mathbf{T}_p = \frac{1}{2}\begin{pmatrix} 1+\eta_p+\xi_p & 1-\eta_p-\xi_p \\ 1-\eta_p+\xi_p & 1+\eta_p-\xi_p \end{pmatrix}. \tag{D17}$$

Here $\mathbf{T}_p$ is a transmission matrix for p-polarized electromagnetic waves. By following the same procedure, a transmission matrix for s-polarized waves (transverse electric waves) is found to be

$$\mathbf{T}_s = \frac{1}{2}\begin{pmatrix} 1+\eta_s+\xi_s & 1-\eta_s+\xi_s \\ 1-\eta_s-\xi_s & 1+\eta_s-\xi_s \end{pmatrix}, \tag{D18}$$

where

$$\eta_s = \frac{k_{2,y}}{k_{1,y}}, \quad \xi_s = \frac{\sigma\mu_0\omega}{k_{1,y}}. \tag{D19}$$

The propagation matrix can easily be derived by recalling the fact that an electromagnetic wave with y component of wave vector k_y propagating through a distance d in the y direction in a uniform medium only changes its phase by $k_y d$. Hence, the propagation matrix is given by

$$\mathbf{P}(d) = \begin{pmatrix} e^{-ik_y d} & 0 \\ 0 & e^{ik_y d} \end{pmatrix}. \tag{D20}$$

Now that we have obtained explicit forms for both transmission and propagation matrices, a transfer matrix for calculating the reflection coefficients can be constructed from a series of matrix multiplications in reverse chronological order of the scattering events that the matrices correspond to. Writing the transfer matrix in the form $\mathbf{M} = \begin{pmatrix} M_{11} & M_{12} \\ M_{21} & M_{22} \end{pmatrix}$, the reflection coefficients can be straightforwardly obtained from two of the matrix elements via

$$r_{s,p} = \frac{M_{21}}{M_{11}}. \tag{D21}$$

For the atom-chip structure shown in Fig. 1, the associated transfer matrix can be written as

$$\mathbf{M} = \mathbf{T}_{\mathrm{hBN}}\mathbf{P}(t_{\mathrm{hBN}})\mathbf{T}_{\mathrm{Gr}}\mathbf{P}(t_{\mathrm{hBN}})\mathbf{T}_{\mathrm{hBN}}, \tag{D22}$$

where $\mathbf{T}_{\mathrm{hBN}}$ and $\mathbf{T}_{\mathrm{Gr}}$ are, respectively, associated with transmission across the hBN interface and the graphene interface, while $\mathbf{P}(t_{\mathrm{hBN}})$ corresponds to propagation through the thickness t_{hBN} of the hBN layer.

APPENDIX E: THREE-BODY LOSS RATE IN 1D BECs

In this Appendix we provide a more detailed derivation of the three-body loss rate considered in the main text, which mainly follows [45,50,51,136]. We start by considering an ^{87}Rb quasicondensate with a mean atomic volume density $\rho_0(\mathbf{r},t)$ at time t, where $\mathbf{r} = (x, y, z)$ denotes the center of a cell of volume Δ, which is small enough for the condensate to be considered homogeneous throughout the cell [i.e., $\partial\rho_0(\mathbf{r},t)/\partial\Delta \approx 0$], but also large enough to accommodate many atoms. Assuming that the condensate is subject to a three-body loss process, its mean volume density evolves in time according to [50,51]

$$\frac{d\rho_0}{dt} = -\kappa_{\mathrm{Rb}}\rho_0^3, \tag{E1}$$

where $\kappa_{\mathrm{Rb}} = 1.8 \times 10^{-41}$ m^6 s^{-1} is the three-body recombination rate for ^{87}Rb atoms in the $F = m_F = 2$ state [52] and we have dropped the explicit dependence of ρ_0 on $(\mathbf{r},t)$ for simplicity. Henceforth, we derive the three-body loss rate at the center of the trap ($z = 0$) for a 1D quasicondensate by integrating the loss rate for a 3D quasicondensate given in Eq. (E1) over the radial coordinate.

However, first let us assume that this condensate is greatly elongated in one dimension, i.e., that it is trapped in a smoothly varying anisotropic harmonic potential with radial trapping frequency $\omega_r = \omega_x = \omega_y$ and axial trapping frequency ω_z, where $\omega_r \gg \omega_z$. Consequently, the density profile of the condensate can be described by a one-dimensional Thomas-Fermi distribution in the z direction, multiplied by the Gaussian ground-state quantum harmonic-oscillator wave functions in the x and y directions [45],

$$\rho_0(r,z) = \frac{1}{U_0}\left(\mu_{\mathrm{eff}} - \frac{m\omega_z^2}{2}z^2\right)e^{-r^2/2a_r^2}, \tag{E2}$$

where $U_0 = 4\pi\hbar^2 a_T/m$, $a_T = 5.6$ nm is the s-wave scattering length [48], $\mu_{\mathrm{eff}} = \mu - \hbar\omega_r$, μ is the chemical potential of the condensate, $m = 1.44 \times 10^{-25}$ kg is the mass of an ^{87}Rb atom, $a_r = \sqrt{\hbar/m\omega_r}$, and $r = \sqrt{x^2 + (y - y_c)^2}$ is the radial distance measured from the mean positions of the harmonic-oscillator states at $x = 0$ and $y = y_c$. It can be seen that in the z direction, the mean volume density peaks at the trap center, where $z = 0$.

We can obtain the mean line density $n_0(z)$ by integrating Eq. (E2) radially from $r = 0$ to $r = \infty$:

$$\begin{aligned}
\int_0^\infty \rho_0 2\pi r\,dr &= \frac{1}{U_0}\left(\mu_{\mathrm{eff}} - \frac{m\omega_z^2}{2}z^2\right)\int_0^\infty e^{-r^2/2a_r^2}2\pi r\,dr,\\
n_0(z) &= \frac{1}{U_0}\left(\mu_{\mathrm{eff}} - \frac{m\omega_z^2}{2}z^2\right)\left[0 + 2\pi a_r^2\right],\\
n_0(z) &= \frac{2\pi a_r^2}{U_0}\left(\mu_{\mathrm{eff}} - \frac{m\omega_z^2}{2}z^2\right).
\end{aligned} \tag{E3}$$

Performing a radial integration on Eq. (E1) in the same manner, we obtain the time evolution of the mean line density as

$$\begin{aligned}
\int_0^\infty \frac{d\rho_0}{dt}2\pi r\,dr &= -\int_0^\infty \kappa_{\mathrm{Rb}}\rho_0^3 2\pi r\,dr,\\
\frac{dn_0(z)}{dt} &= -\frac{\kappa_{\mathrm{Rb}}}{12\pi^2 a_r^4}n_0(z)^3,
\end{aligned} \tag{E4}$$

where we have used Eqs. (E2) and (E3) to convert from a volume to a line atomic density.

[1] I. Bloch, J. Dalibard, and W. Zwerger, Rev. Mod. Phys. **80**, 885 (2008).

[2] C. L. Degen, F. Reinhard, and P. Cappellaro, Rev. Mod. Phys. **89**, 035002 (2017).

[3] Y. Bidel, O. Carraz, R. Charrière, M. Cadoret, N. Zahzam, and A. Bresson, Appl. Phys. Lett. **102**, 144107 (2013).

[4] S. Bize, P. Laurent, M. Abgrall, H. Marion, I. Maksimovic, L. Cacciapuoti, J. Grünert, C. Vian, F. Pereira dos Santos, P. Rosenbusch, P. Lemonde, G. Santarelli, P. Wolf, A. Clairon, A. Luiten, M. Tobar, and C. Salomon, J. Phys. B **38**, S449 (2005).

[5] T. L. Gustavson, P. Bouyer, and M. A. Kasevich, Phys. Rev. Lett. **78**, 2046 (1997).

[6] J. D. Elgin, T. P. Heavner, J. Kitching, E. A. Donley, J. Denney, and E. A. Salim, Appl. Phys. Lett. **115**, 033503 (2019).

[7] S. Wildermuth, S. Hofferberth, I. Lesanovsky, E. Haller, L. M. Andersson, S. Groth, I. Bar-Joseph, P. Krüger, and J. Schmiedmayer, Nature (London) **435**, 440 (2005).

[8] S. Wildermuth, S. Hofferberth, I. Lesanovsky, S. Groth, P. Krüger, J. Schmiedmayer, and I. Bar-Joseph, Appl. Phys. Lett. **88**, 264103 (2006).

[9] S. Hofferberth, P. Krüger, S. Schmiedmayer, and S. Wildermuth, German Patent No. DE102005023937A1 (2006) (23 November 2006), https://depatisnet.dpma.de/DepatisNet/depatisnet?action=bibdat.

[10] M. V. Romalis, Nat. Photon. **1**, 613 (2007).

[11] B. Dellabetta, T. L. Hughes, M. J. Gilbert, and B. L. Lev, Phys. Rev. B **85**, 205442 (2012).

[12] F. Yang, A. J. Kollár, S. F. Taylor, R. W. Turner, and B. L. Lev, Phys. Rev. Appl. **7**, 034026 (2017).

[13] V. Shah, J. Osborne, J. Orton, and O. Alem, in *Steep Dispersion Engineering and Opto-Atomic Precision Metrology XI*, edited by S. M. Shahriar and J. Scheuer, SPIE Proc. Vol. 10548 (SPIE, Bellingham, 2018), p. 51.

[14] S. Taylor, F. Yang, B. Freudenstein, and B. Lev, SciPost Phys. **10**, 060 (2021).

[15] P. Knight and I. Walmsley, Quantum Sci. Technol. **4**, 040502 (2019).

[16] A. Acín, I. Bloch, H. Buhrman, T. Calarco, C. Eichler, J. Eisert, D. Esteve, N. Gisin, S. Glaser, F. Jelezko, S. Kuhr, M. Lewenstein, M. Riedel, P. Schmidt, R. Thew, A. Wallraff, I. Walmsley, and F. Wilhelm, New J. Phys. **20**, 080201 (2018).

[17] R. Folman, P. Kruger, J. Schmiedmayer, J. hecker denschlag, and C. Henkel, Adv. At. Mol. Opt. Phys. **48**, 263 (2002).

[18] J. Fortágh and C. Zimmermann, Rev. Mod. Phys. **79**, 235 (2007).

[19] H. Ott, J. Fortagh, G. Schlotterbeck, A. Grossmann, and C. Zimmermann, Phys. Rev. Lett. **87**, 230401 (2001).

[20] W. Hänsel, P. Hommelhoff, T. W. Hänsch, and J. Reichel, Nature (London) **413**, 498 (2001).

[21] T. Schumm, S. Hofferberth, L. M. Andersson, S. Wildermuth, S. Groth, I. Bar-Joseph, J. Schmiedmayer, and P. Krüger, Nat. Phys. **1**, 57 (2005).

[22] Y.-J. Wang, D. Z. Anderson, V. M. Bright, E. A. Cornell, Q. Diot, T. Kishimoto, M. Prentiss, R. A. Saravanan, S. R. Segal, and S. Wu, Phys. Rev. Lett. **94**, 090405 (2005).

[23] D. Hunger, S. Camerer, T. W. Hänsch, D. König, J. P. Kotthaus, J. Reichel, and P. Treutlein, Phys. Rev. Lett. **104**, 143002 (2010).

[24] P. Schneeweiss, M. Gierling, G. Visanescu, D. P. Kern, T. E. Judd, A. Günther, and J. Fortágh, Nat. Nanotechnol. **7**, 515 (2012).

[25] P. G. Petrov, S. Machluf, S. Younis, R. Macaluso, T. David, B. Hadad, Y. Japha, M. Keil, E. Joselevich, and R. Folman, Phys. Rev. A **79**, 043403 (2009).

[26] C. Hufnagel, T. Mukai, and F. Shimizu, Phys. Rev. A **79**, 053641 (2009).

[27] V. Dikovsky, V. Sokolovsky, B. Zhang, C. Henkel, and R. Folman, Eur. Phys. J. D **51**, 247 (2009).

[28] T. Nirrengarten, A. Qarry, C. Roux, A. Emmert, G. Nogues, M. Brune, J.-M. Raimond, and S. Haroche, Phys. Rev. Lett. **97**, 200405 (2006).

[29] C. Roux, A. Emmert, A. Lupascu, T. Nirrengarten, G. Nogues, M. Brune, J.-M. Raimond, and S. Haroche, Europhys. Lett. **81**, 56004 (2008).

[30] D. Cano, H. Hattermann, B. Kasch, C. Zimmermann, R. Kleiner, D. Koelle, and J. Fortágh, Eur. Phys. J. D **63**, 17 (2011).

[31] S. Minniberger, F. Diorico, S. Haslinger, C. Hufnagel, C. Novotny, N. Lippok, J. Majer, C. Koller, S. Schneider, and J. Schmiedmayer, Appl. Phys. B **116**, 1017 (2014).

[32] C. Henkel, P. Krüger, R. Folman, and J. Schmiedmayer, Appl. Phys. B **76**, 173 (2003).

[33] Y.-j. Lin, I. Teper, C. Chin, and V. Vuletić, Phys. Rev. Lett. **92**, 050404 (2004).

[34] E. Vetsch, D. Reitz, G. Sagué, R. Schmidt, S. T. Dawkins, and A. Rauschenbeutel, Phys. Rev. Lett. **104**, 203603 (2010).

[35] P. Schneeweiss, F. L. Kien, and A. Rauschenbeutel, New J. Phys. **16**, 013014 (2014).

[36] Y. Wang, T. Tran, P. Surendran, I. Herrera, A. Balcytis, D. Nissen, M. Albrecht, A. Sidorov, and P. Hannaford, Phys. Rev. A **96**, 013630 (2017).

[37] Y. Meng, A. Dareau, P. Schneeweiss, and A. Rauschenbeutel, Phys. Rev. X **8**, 031054 (2018).

[38] T. David, Y. Japha, V. Dikovsky, R. Salem, C. Henkel, and R. Folman, Eur. Phys. J. D **48**, 321 (2008).

[39] J. Verdú, H. Zoubi, C. Koller, J. Majer, H. Ritsch, and J. Schmiedmayer, Phys. Rev. Lett. **103**, 043603 (2009).

[40] S. Bernon, H. Hattermann, D. Bothner, M. Knufinke, P. Weiss, F. Jessen, D. Cano, M. Kemmler, R. Kleiner, D. Koelle, and J. Fortágh, Nat. Commun. **4**, 2380 (2013).

[41] G. Sinuco-León, B. Kaczmarek, P. Krüger, and T. M. Fromhold, Phys. Rev. A **83**, 021401(R) (2011).

[42] G. Sinuco-León, P. Krüger, and T. Fromhold, J. Mod. Opt. **65**, 677 (2018).

[43] A. K. Geim and I. V. Grigorieva, Nature (London) **499**, 419 (2013).

[44] M. Yankowitz, Q. Ma, P. Jarillo-Herrero, and B. LeRoy, Nat. Rev. Phys. **1**, 112 (2019).

[45] C. J. Pethick and H. Smith, *Bose-Einstein Condensation in Dilute Gases*, 2nd ed. (Cambridge University Press, Cambridge, 2008).

[46] M. Olshanii, Phys. Rev. Lett. **81**, 938 (1998).

[47] C. Menotti and S. Stringari, Phys. Rev. A **66**, 043610 (2002).

[48] J. L. Roberts, N. R. Claussen, J. P. Burke, C. H. Greene, E. A. Cornell, and C. E. Wieman, Phys. Rev. Lett. **81**, 5109 (1998).

[49] D. A. Smith, S. Aigner, S. Hofferberth, M. Gring, M. Andersson, S. Wildermuth, P. Krüger, S. Schneider, T. Schumm, and K. Schmiedmayer, Opt. Express **19**, 8471 (2011).

[50] I. Bouchoule, M. Schemmer, and C. Henkel, SciPost Phys. **5**, 43 (2018).

[51] M. Schemmer and I. Bouchoule, Phys. Rev. Lett. **121**, 200401 (2018).

[52] J. Söding, D. Guéry-Odelin, P. Desbiolles, F. Chevy, H. Inamori, and J. Dalibard, Appl. Phys. B **69**, 257 (1999).

[53] B. Standley, W. Bao, H. Zhang, J. Bruck, C. Lau, and M. Bockrath, Nano Lett. **8**, 3345 (2008).

[54] S. Hertel, F. Kisslinger, J. Jobst, D. Waldmann, M. Krieger, and H. Weber, Appl. Phys. Lett. **98**, 212109 (2011).

[55] K. Bolotin, K. Sikes, Z. Jiang, M. Klima, G. Fudenberg, J. Hone, P. Kim, and H. Stormer, Solid State Commun. **146**, 351 (2008).

[56] R. V. Gorbachev, I. Riaz, R. R. Nair, R. Jalil, L. Britnell, B. D. Belle, E. W. Hill, K. S. Novoselov, K. Watanabe, T. Taniguchi, A. K. Geim, and P. Blake Small **7**, 465 (2011).

[57] A. Summerfield, A. Davies, T. S. Cheng, V. V. Korolkov, Y. Cho, C. J. Mellor, C. T. Foxon, A. N. Khlobystov, K. Watanabe, T. Taniguchi, L. Eaves, S. V. Novikov, and P. H. Beton, Sci. Rep. **6**, 22440 (2016).

[58] A. Summerfield, A. Davies, T. S. Cheng, V. V. Korolkov, Y. J. Cho, C. J. Mellor, C. T. Foxon, A. N. Khlobystov, K. Watanabe, T. Taniguchi, L. Eaves, S. V. Novikov, and P. H. Beton, Sci. Rep. **6**, 27047 (2016).

[59] Y.-J. Cho, A. Summerfield, A. Davies, T. S. Cheng, E. F. Smith, C. J. Mellor, A. N. Khlobystov, C. T. Foxon, L. Eaves, P. H. Beton, and S. V. Novikov, Sci. Rep. **6**, 34474 (2016).

[60] C. Stampfera, J. Güttinger, F. Molitor, D. Graf, T. Ihn, and K. Ensslin, Appl. Phys. Lett. **92**, 012102 (2008).

[61] G. Kim, S.-S. Kim, J. Jeon, S. I. Yoon, S. Hong, Y. J. Cho, A. Misra, S. Ozdemir, J. Yin, D. Ghazaryan, M. Holwill, A. Mishchenko, D. V. Andreeva, Y.-J. Kim, H. Y. Jeong, A.-R. Jang, H.-J. Chung, A. K. Geim, K. S. Novoselov, B.-H. Sohn, and H. S. Shin, Nat. Commun. **10**, 230 (2019).

[62] M. M. Khan, S. Ribeiro, J. T. Mendonça, and H. Terças, Phys. Rev. A **102**, 033115 (2020).
[63] H. B. G. Casimir and D. Polder, Phys. Rev. **73**, 360 (1948).
[64] J. M. Wylie and J. E. Sipe, Phys. Rev. A **30**, 1185 (1984).
[65] M. P. A. Jones, C. J. Vale, D. Sahagun, B. V. Hall, and E. A. Hinds, Phys. Rev. Lett. **91**, 080401 (2003).
[66] D. M. Harber, J. M. McGuirk, J. M. Obrecht, and E. A. Cornell, J. Low Temp. Phys. **133**, 229 (2003).
[67] S. Y. Buhmann and S. Scheel, Phys. Rev. Lett. **100**, 253201 (2008).
[68] F. Intravaia, C. Henkel, and M. Antezza, *Fluctuation-Induced Forces between Atoms and Surfaces: The Casimir-Polder Interaction* (Springer, Berlin, 2011), pp. 345–391.
[69] T. Matsubara, Prog. Theor. Phys. **14**, 351 (1955).
[70] A. Yariv and P. Yeh, *Optical Waves in Crystals* (Wiley, New York, 1983), Vol. 5.
[71] T. Zhan, X. Shi, Y. Dai, X. Liu, and J. Zi, J. Phys.: Condens. Matter **25**, 215301 (2013).
[72] T. Gric, Opt. Quantum Electron. **51**, 202 (2019).
[73] A. Andryieuski and A. V. Lavrinenko, Opt. Express **21**, 9144 (2013).
[74] P. A. D. Gonçalves and N. M. R. Peres, *An Introduction to Graphene Plasmonics* (World Scientific, Singapore, 2016).
[75] B. Amorim, P. A. D. Gonçalves, M. I. Vasilevskiy, and N. M. R. Peres, Appl. Sci. **7**, 1158 (2017).
[76] L. Ju, B. Geng, J. Horng, C. Girit, M. Martin, Z. Hao, H. A. Bechtel, X. Liang, A. Zettl, Y. R. Shen, and F. Wang, Nat. Nanotechnol. **6**, 630 (2011).
[77] T. E. Judd, R. G. Scott, A. M. Martin, B. Kaczmarek, and T. M. Fromhold, New J. Phys. **13**, 083020 (2011).
[78] P. Schwerdtfeger and J. K. Nagle, Mol. Phys. **117**, 1200 (2018).
[79] D. A. Steck, Alkali D line data, revision 2.2.1, available at http://steck.us/alkalidata/ (2019).
[80] Y. V. Churkin, A. B. Fedortsov, G. L. Klimchitskaya, and V. A. Yurova, Phys. Rev. B **82**, 165433 (2010).
[81] M. Bordag, B. Geyer, G. L. Klimchitskaya, and V. M. Mostepanenko, Phys. Rev. B **74**, 205431 (2006).
[82] G. L. Klimchitskaya, U. Mohideen, and V. M. Mostepanenko, Rev. Mod. Phys. **81**, 1827 (2009).
[83] S. Ribeiro and S. Scheel, Phys. Rev. A **88**, 042519 (2013).
[84] M. Antezza, I. Fialkovsky, and N. Khusnutdinov, Phys. Rev. B **102**, 195422 (2020).
[85] G. L. Klimchitskaya and V. M. Mostepanenko, Universe **6**, 150 (2020).
[86] R. Salem, Y. Japha, J. Chabé, B. Hadad, M. Keil, K. A. Milton, and R. Folman, New J. Phys. **12**, 023039 (2010).
[87] E. Harper and D. Anderson, in *The George Gamow Symposium*, edited by E. Harper, W. C. Parke, and G. D. Anderson, Astronomical Society of the Pacific Conference Series Vol. 129 (Astronomical Society of the Pacific, San Francisco, 1997), p. 29.
[88] R. Shankar, *Principles of Quantum Mechanics*, 2nd ed. (Plenum, New York, 2011).
[89] B. M. Karnakov and V. P. Krainov, *WKB Approximation in Atomic Physics* (Springer, Berlin, 2013).
[90] D. J. Griffiths, *Introduction to Quantum Mechanics*, 2nd ed. (Pearson Prentice Hall, Upper Saddle River, 2005).
[91] C. Henkel, S. Pötting, and M. Wilkens, Appl. Phys. B **69**, 379 (1999).
[92] C. Henkel and S. Pötting, Appl. Phys. B **72**, 73 (2001).
[93] T. Fang, A. Konar, H. Xing, and D. Jena, Appl. Phys. Lett. **91**, 092109 (2007).
[94] K. I. Bolotin, K. J. Sikes, J. Hone, H. L. Stormer, and P. Kim, Phys. Rev. Lett. **101**, 096802 (2008).
[95] J.-H. Chen, C. Jang, S. Xiao, M. Ishigami, and M. S. Fuhrer, Nat. Nanotechnol. **3**, 206 (2008).
[96] K. H. J. Buschow and F. R. de Boer, *Physics of Magnetism and Magnetic Materials* (World Publishing, Beijing, 2013).
[97] P. K. Rekdal, S. Scheel, P. L. Knight, and E. A. Hinds, Phys. Rev. A **70**, 013811 (2004).
[98] L. Novotny and B. Hecht, *Principles of Nano-Optics*, 1st ed. (Cambridge University Press, New York, 2006).
[99] S. Buhmann, *Dispersion Forces II: Many-Body Effects, Excited Atoms, Finite Temperature and Quantum Friction*, Springer Tracts in Modern Physics Vol. 248 (Springer, Berlin, 2012).
[100] N. Zettili, *Quantum Mechanics: Concepts and Applications*, 2nd ed. (Wiley, New York, 2009).
[101] M. Maqbool and T. Khan, Surf. Rev. Lett. **12**, 759 (2005).
[102] P. Krüger, L. M. Andersson, S. Wildermuth, S. Hofferberth, E. Haller, S. Aigner, S. Groth, I. Bar-Joseph, and J. Schmiedmayer, Phys. Rev. A **76**, 063621 (2007).
[103] T. Schumm, J. Estève, C. Figl, J.-B. Trebbia, C. Aussibal, H. Nguyen, D. Mailly, I. Bouchoule, C. I. Westbrook, and A. Aspect, Eur. Phys. J. D **32**, 171 (2005).
[104] D.-W. Wang, M. D. Lukin, and E. Demler, Phys. Rev. Lett. **92**, 076802 (2004).
[105] J. D. Thomsen, T. Gunst, S. S. Gregersen, L. Gammelgaard, B. S. Jessen, D. M. A. Mackenzie, K. Watanabe, T. Taniguchi, P. Bøggild, and T. J. Booth, Phys. Rev. B **96**, 014101 (2017).
[106] C. R. Dean, A. F. Young, I. Meric, C. Lee, L. Wang, S. Sorgenfrei, K. Watanabe, T. Taniguchi, P. Kim, K. L. Shepard, and J. Hone, Nat. Nanotechnol. **5**, 722 (2010).
[107] R. Decker, Y. Wang, V. W. Brar, W. Regan, H.-Z. Tsai, Q. Wu, W. Gannett, A. Zettl, and M. F. Crommie, Nano Lett. **11**, 2291 (2011).
[108] J. Xue, J. Sanchez-Yamagishi, D. Bulmash, P. Jacquod, A. Deshpande, K. Watanabe, T. Taniguchi, P. Jarillo-Herrero, and B. J. LeRoy, Nat. Mater. **10**, 282 (2011).
[109] W. Xu and T.-W. Lee, Mater. Horiz. **3**, 186 (2016).
[110] S. Aigner, L. D. Pietra, Y. Japha, O. Entin-Wohlman, T. David, R. Salem, R. Folman, and J. Schmiedmayer, Science **319**, 1226 (2008).
[111] Y. Japha, O. Entin-Wohlman, T. David, R. Salem, S. Aigner, J. Schmiedmayer, and R. Folman, Phys. Rev. B **77**, 201407(R) (2008).
[112] L. Britnell, R. V. Gorbachev, A. K. Geim, L. A. Ponomarenko, A. Mishchenko, M. T. Greenaway, T. M. Fromhold, K. S. Novoselov, and L. Eaves, Nat. Commun. **4**, 1794 (2013).
[113] J. Martin, N. Akerman, G. Ulbricht, T. Lohmann, J. H. Smet, K. von Klitzing, and A. Yacoby, Nat. Phys. **4**, 144 (2007).
[114] Q. Li, E. H. Hwang, E. Rossi, and S. Das Sarma, Phys. Rev. Lett. **107**, 156601 (2011).
[115] J. Yan and M. S. Fuhrer, Phys. Rev. Lett. **107**, 206601 (2011).
[116] M. Yankowitz, J. Xue, D. Cormode, J. D. Sanchez-Yamagishi, K. Watanabe, T. Taniguchi, P. Jarillo-Herrero, P. Jacquod, and B. J. LeRoy, Nat. Phys. **8**, 382 (2012).

[117] M. T. Greenaway, E. E. Vdovin, A. Mishchenko, O. Makarovsky, A. Patanè, J. R. Wallbank, Y. Cao, A. V. Kretinin, M. J. Zhu, S. V. Morozov, V. I. Fal'ko, K. S. Novoselov, A. K. Geim, T. M. Fromhold, and L. Eaves, Nat. Phys. **11**, 1057 (2015).

[118] A. Davies, J. D. Albar, A. Summerfield, J. C. Thomas, T. S. Cheng, V. V. Korolkov, E. Stapleton, J. Wrigley, N. L. Goodey, C. J. Mellor, A. N. Khlobystov, K. Watanabe, T. Taniguchi, C. T. Foxon, L. Eaves, S. V. Novikov, and P. H. Beton, Nano Lett. **18**, 498 (2017).

[119] C. Tai, *Dyadic Green Functions in Electromagnetic Theory*, 2nd ed. (IEEE, Piscataway, 1994).

[120] J. A. Crosse, S. Fuchs, and S. Y. Buhmann, Phys. Rev. A **92**, 063831 (2015).

[121] L. A. Falkovsky, J. Phys.: Conf. Ser. **129**, 012004 (2008).

[122] I. V. Fialkovsky, V. N. Marachevsky, and D. V. Vassilevich, Phys. Rev. B **84**, 035446 (2011).

[123] C. H. Egerland, K. Busch, and F. Intravaia, Phys. Rev. B **100**, 235418 (2019).

[124] J. F. M. Werra, P. Krüger, K. Busch, and F. Intravaia, Phys. Rev. B **93**, 081404(R) (2016).

[125] C. Henkel, G. L. Klimchitskaya, and V. M. Mostepanenko, Phys. Rev. A **97**, 032504 (2018).

[126] S.-A. Biehs and G. S. Agarwal, Phys. Rev. A **90**, 042510 (2014).

[127] T. Stauber, N. M. R. Peres, and A. K. Geim, Phys. Rev. B **78**, 085432 (2008).

[128] G. W. Hanson, J. Appl. Phys. **113**, 029902 (2013).

[129] M. Y. Musa, M. Renuka, X. Lin, R. Li, H. Wang, E. Li, B. Zhang, and H. Chen, 2D Mater. **5**, 015018 (2018).

[130] S. C. Lee, S. S. Ng, H. Abu Hassan, Z. Hassan, and T. Dumelow, Opt. Mater. (Amsterdam) **37**, 773 (2014).

[131] A. Woessner, M. B. Lundeberg, Y. Gao, A. Principi, P. Alonso-González, M. Carrega, K. Watanabe, T. Taniguchi, G. Vignale, M. Polini, J. Hone, R. Hillenbrand, and F. H. L. Koppens, Nat. Mater. **14**, 421 (2014).

[132] F. Gervais and B. Piriou, J. Phys. C **7**, 2374 (1974).

[133] Y. Cai, L. Zhang, Q. Zeng, L. Cheng, and Y. Xu, Solid State Commun. **141**, 262 (2007).

[134] T. Okamoto, Top. Appl. Phys. **81**, 97 (2001).

[135] B. Zhang, C. Henkel, E. Haller, S. Wildermuth, S. Hofferberth, P. Krüger, and J. Schmiedmayer, Eur. Phys. J. D **35**, 97 (2005).

[136] D. S. Petrov, D. M. Gangardt, and G. V. Shlyapnikov, J. Phys. (France) IV **116**, 5 (2004).